This is to certify that the

dissertation entitled

GRAVITATIONAL LENSING DEPLETION IN THE NOAO DEEP WIDE FIELD

presented by

MICHAEL WAYNE DAVIS

has been accepted towards fulfillment
of the requirements for

Ph.D. degree in Astrophysics

Major professor

Date December 5, 2002

GRAVITATIONAL LENSING DEPLETION IN THE NOAO DEEP WIDE FIELD

By

MICHAEL WAYNE DAVIS

A DISSERTATION

Submitted to
Michigan State University
in partial fulfillment of the requirements
for the degree of

DOCTOR OF PHILOSOPHY

Department of Physics and Astronomy

2002

ABSTRACT

GRAVITATIONAL LENSING DEPLETION IN THE NOAO DEEP WIDE FIELD

By

MICHAEL WAYNE DAVIS

A new method to measure mass of a sample of field galaxies is proposed. The mass of foreground galaxies may be estimated by measuring the reduction in the density of surrounding background galaxies. The reduction in number density is due to gravitational lensing depletion.

A foreground mass acts as a gravitational lens and will magnify the background area surrounding the mass. This magnification lowers the number density of background galaxies found behind the mass. One can use the reduction in number density to calculate the rotation velocity of the foreground galaxies.

To demonstrate this method, photometry is performed on four $0.5^\circ \times 0.5^\circ$ fields from the NOAO Deep Wide Field survey. Photometric redshifts are derived from the photometry. The results are placed in a catalogue for public access.

Red foreground galaxies ($B-V \geq 0.61$) have a mean rotation velocity of 308 ± 30 km/s, while blue foreground galaxies ($B-V < 0.61$) have a mean rotation velocity of 210 ± 35 km/s. The rotation velocities of red galaxies with $B > 22$ and $B < 22$ and the Tully-Fisher relation suggest a magnitude difference of 1.7 ± 0.4. The real magnitude difference is 1.9, consistent with the difference estimated from the Tully-Fisher relation. The rotation velocity difference between red galaxies at redshift $z = 0.2$ and $z = 0.5$ is 22 ± 44 km/s, consistent with zero. The rotation velocity difference between blue galaxies at the same redshifts is 17 ± 49 km/s, also consistent with zero. This measurement is the first direct measurement of the rotation velocity of distant blue galaxies.

Acknowledgements

This work made use of images and/or data products provided by the NOAO Deep Wide-Field Survey, which is supported by the National Optical Astronomy Observatory (NOAO). NOAO is operated by AURA, Inc., under a cooperative agreement with the National Science Foundation.

First, I would like to thank my advisor Prof. Edwin D. Loh. I have learned more about astronomy and instrumentation under his guidance than I can imagine learning from any other two advisors combined.

Second, I would like to thank Aaron "Cluze" LaCluyzé for the assistance provided during this research. I am especially grateful for the use of fornax to run SExtractor.

I thank Karen Kinemuchi, Brian Marsteller, Brian Sharpee, and Chris Waters for listening to my explanations and checking my reasoning while preparing this dissertation. Thanks also goes to Jason Biel, Karen, and Cluze for help with LaTeX.

A special thank you goes to Dr. Robert Slater for assistance with meeting MSU dissertation formatting requirements.

More thanks go to Ryan Kruse, Cluze, Dr. Charles Moreau, Dr. Peter Peterson, Dr. Frédéric Pierre, Dr. Slater, and the rest of the gaming-and-trivia crowd for large doses of stress relief.

A huge thank you goes to my wife Jennifer and son Jonathan for putting up with my absences and living in Spartan Village while completing this work.

Finally, and most importantly, I would like to thank YHWH for creating this universe and giving me a chance to study it.

Table of Contents

List of Tables

List of Figures

Chapter 1

Introduction

1.1 Motivation

An important area of astrophysics is the study of the evolution of galaxies. While basic properties of nearby galaxies are known, it is more difficult to determine those properties for distant (and older) galaxies. More importantly, it is uncertain whether such properties as mass and luminosity change as galaxies age.

The goal of this research is to determine if the masses of red and blue galaxies change with age. Gravitational lensing depletion is the tool used to make this measurement. A brief summary of the history and application of gravitational lensing follows.

1.2 Gravitational Lensing

1.2.1 Overview

Gravitational lensing occurs when light rays are bent by a massive object [8]. Figure 1.1 shows a basic diagram of gravitational lensing. The apparent position of the background object is moved away from the lensing object because of gravitational

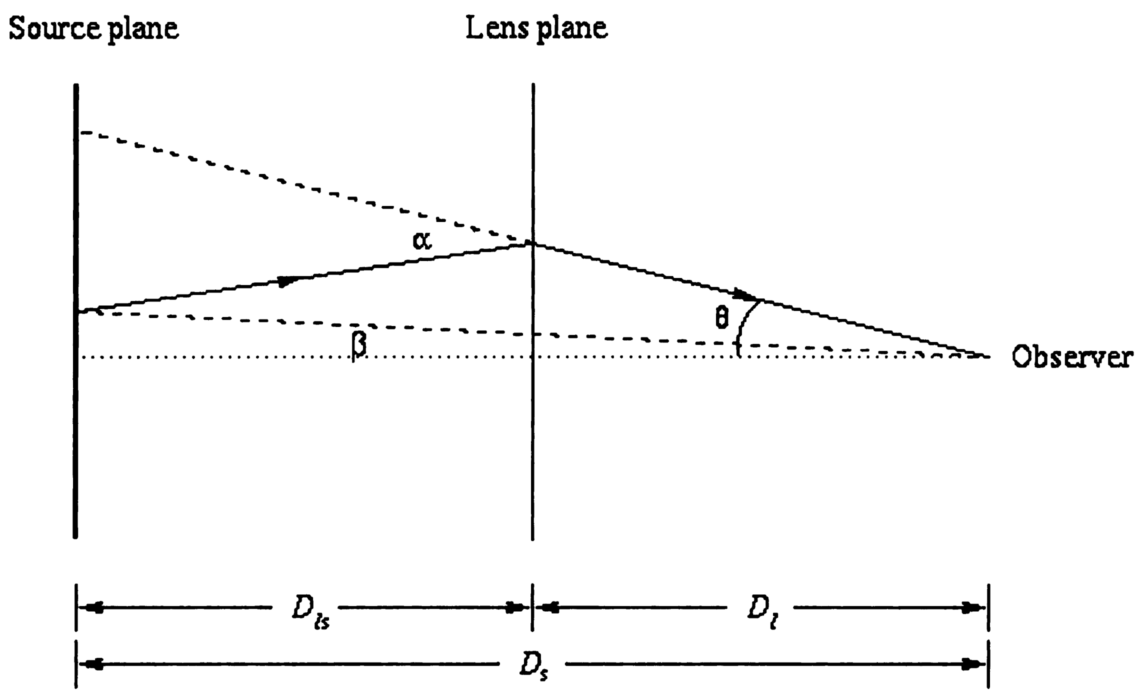

Figure 1.1: Diagram of gravitational lensing. The effective position of the background object is moved away from the lens.

bending. If a lensing object is placed in front of a field of objects, the number of background objects surrounding the lens will diminish. This effect is known as gravitational lensing depletion, or magnification bias. The shape of the background objects will also distort so that they appear slightly elongated in the radial direction. This effect is referred to as shape distortion or weak gravitational lensing.

Gravitational lensing depletion may only be measured if the baseline number density of background galaxies is known. Foreground galaxies mixed with background galaxies will contaminate the lensing signal. Also, minor fluctuations in background density can affect the measured signal if the area covered by the background sample is not large. Therefore, to measure gravitational lensing depletion, one must observe a large area of the sky and somehow obtain good separation between foreground and background galaxies. The difficulty in meeting both conditions has kept the number of gravitational lensing depletion measurements small.

Tyson [28] first measured gravitational light deflection by foreground galaxies in 1984. They measured the shape distortion of 46,954 galaxies near 11,789 foreground galaxies. Their images came from photographic plates with a minimum resolvable angular separation of 20 arcseconds. Lacking redshift data, they also separated foreground galaxies from background galaxies by flux.

Brainerd, Blandford, & Smail measured the shape distortion in 1996 [3]. Using CCD technology they were able to measure the shape distortion of 3202 pairs of galaxies with angular separations between 5 and 34 arcseconds. They measured an average galactic rotation velocity of 220 ± 80 km/s. Again, foreground galaxies were separated from background galaxies by flux.

Fort *et al.* first measured a magnification bias around Cl0024+1654 [12]. They used the measured bias to constrain the redshift distribution of the background galaxies. Taylor *et al.* used Fort's technique to measure the mass of cluster Abell 1689 [26].

Wilson *et al.* first used galaxy-galaxy lensing to measure the rotation velocity of bright elliptical galaxies [30]. This rotation velocity measurement was derived from the shape distortion of background galaxies surrounding bright elliptical foreground galaxies. They used two-color photometry to separate bright elliptical foreground galaxies from background galaxies and determine the redshifts of the foreground galaxies. The background galaxy redshifts were inferred from their flux. They measured a rotation velocity of 269^{+34}_{-39} km/s for bright elliptical galaxies assuming an Einstein-deSitter cosmology.

1.2.2 Mathematics of Gravitational Lensing Depletion

The galaxy depletion due to gravitational lensing magnification follows the function [4]:

$$\frac{N}{N_0} - 1 = \mu^{2.5\alpha - 1} - 1 \tag{1.1}$$

The left hand side is the angular correlation between the lens and the background galaxies. The background density of galaxies surrounding the lens is N, while the background density of galaxies for the image is N_0. The $\frac{1}{\mu}$ factor is the reduction of the density of background galaxies due to gravitational lensing. The parameter α is the change in number of background galaxies with magnitude, or:

$$\alpha = \frac{d \log N}{dm} \tag{1.2}$$

This parameter represents the magnification of background galaxies due to gravitational lensing. In most cases, $2.5\alpha < 1$, so gravitational lensing causes a net depletion in the number density of background galaxies.

The parameter μ is the gravitational lensing magnification factor. Galaxies have flat rotation curves beyond a few kpc, so the mass distribution has the form $\rho_m \propto r^{-2}$. This mass distribution leads to [22]:

$$\mu = \frac{1}{1 - \frac{R_{\mathrm{E}}}{r}} \tag{1.3}$$

The projected separation between the lens and the background object is r, while the Einstein radius of the lens is R_{E}. Assuming $\frac{R_{\mathrm{E}}}{r}$ is small, $\mu^{2.5\alpha-1}$ reduces to $1-(2.5\alpha-1)\frac{R_{\mathrm{E}}}{r}$. The right hand side of Equation 1.1 then reduces to $(2.5\alpha-1)\frac{R_{\mathrm{E}}}{r}$. There is a degeneracy in α and R_{E}, so both quantities can not be derived solely from the measured depletion.

The Einstein radius has the form [23]:

$$R_{\mathrm{E}} = \sqrt{4\pi \frac{GM}{c^2} \frac{D_{\mathrm{LS}} D_{\mathrm{OL}}}{D_{\mathrm{OS}}}} \tag{1.4}$$

The rotation velocity is constant, so $\frac{GM}{r^2} = \frac{v^2}{r}$ for any value of r. Substituting for GM and $r = R_{\mathrm{E}}$ yields:

$$R_{\mathrm{E}} = 4\pi \frac{v^2}{c^2} \frac{D_{\mathrm{LS}} D_{\mathrm{OL}}}{D_{\mathrm{OS}}} \tag{1.5}$$

D_{LS} is the luminosity distance from the lens to the background source, D_{OL} is the luminosity distance from the observer to the lens, and D_{OS} is the luminosity distance from the observer to the background source. The rotation velocity of the lensing object is v.

The depletion is measured as a function of angular distance from the lens. Equation 1.1 is fit to the depletion, and the best fit value of R_{E} is found. Once R_{E}, the distance to the lens, and the distance to the background are known, the rotation velocity of the lensing object may be calculated.

Young *et al.* show that for a spherically symmetric mass distribution, the deflection of light is only dependent on the mass enclosed within the measurement radius [31]. Therefore, the mass of the lensing object within a given radius may be calculated from the rotation velocity. However, the rotation velocity can only be measured out to the angular distance for which a depletion signal is measured. Therefore, if the object extends beyond the radius for which a measurable signal exists, the rotation velocity only limits the mass within the radius of the signal.

1.3 This Work

This research uses galaxy-galaxy lensing depletion to calculate galactic rotation velocity and, indirectly, mass. The data set is three color photometry in the NOAO Deep Wide Field.

Once photometry is performed photometric redshifts are calculated for the objects in the Deep Wide Field. The calculation of photometric redshifts allows a separation of foreground and background galaxies. Three color photometry also allows the fitting of galaxy type templates to the observations. These procedures are described in Chapter 2.

Once photometric redshifts are determined, the galaxies are split into foreground and background bins. The foreground bins are further separated by color. Then, the depletion in the number of background galaxies surrounding the foreground galaxies may be measured. This depletion is used to calculate the rotation velocity of the foreground galaxies. These procedures are described in Chapter 3.

Chapter 2

Photometry and Photometric Redshifts of the NOAO Deep Wide Field

2.1 Background

The NOAO Deep Wide Field (hereafter referred to as DWF) survey provides the data set upon which this work is based. The DWF images were taken with the 8192×8192 pixel MOSAIC camera on the 4-meter telescope at Kitt Peak National Observatory [15]. The images were taken in a wide blue filter (340 to 490 nm, dubbed Bw), a red filter (550 to 800 nm, dubbed R), and a very near-IR filter (700 to 950 nm, dubbed I). The first data release of the DWF consists of four 36 by 36 arcminute fields near the constellation Boötes. The pixels are 0.258 arcseconds wide. The data were released to the public in January 2001.

The original image processing was performed by Januzzi and Dey [15]. The images were flat-fielded, bias subtracted, and combined into final composite images. They placed the pixel scale, image seeing, gain, position solutions, and photometric

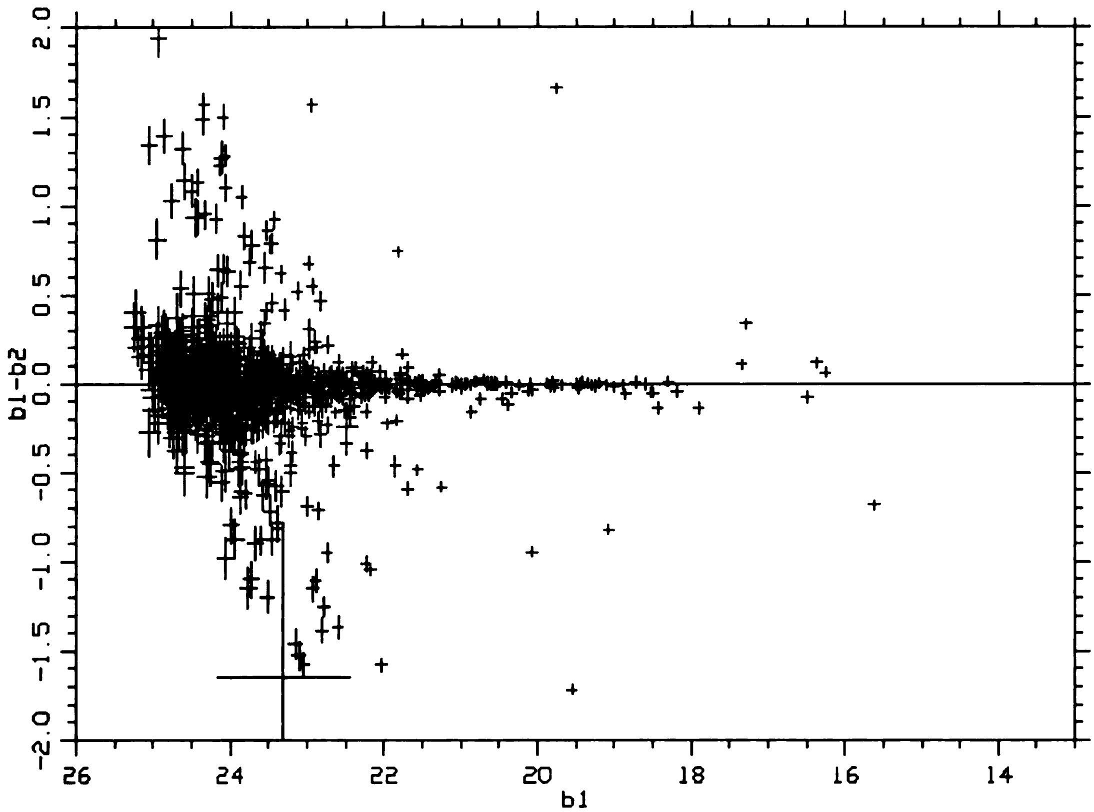

Figure 2.1: The Bw-magnitude difference between DWF frame 1 (b1) and DWF frame 2 (b2) plotted against magnitude of frame 1 (b1). There are over 900 objects in common between the two frames.

zeropoints in the image header. The photometric zeropoint of each image is good to 0.01 magnitudes while the comparison between colors is good to about 0.03 magnitudes [16].

2.2 Photometry Results

The methods used to perform photometry and photometric redshifts are described in Appendix A. These techniques are applied to the four frames of the DWF. The Bw-band images are used as the fiducial source maps due to their low sky background. The only other modification to the technique of Appendix A is the use of 32 $\times$ 32 pixel squares to measure background instead of 72 $\times$ 72. This reduced background

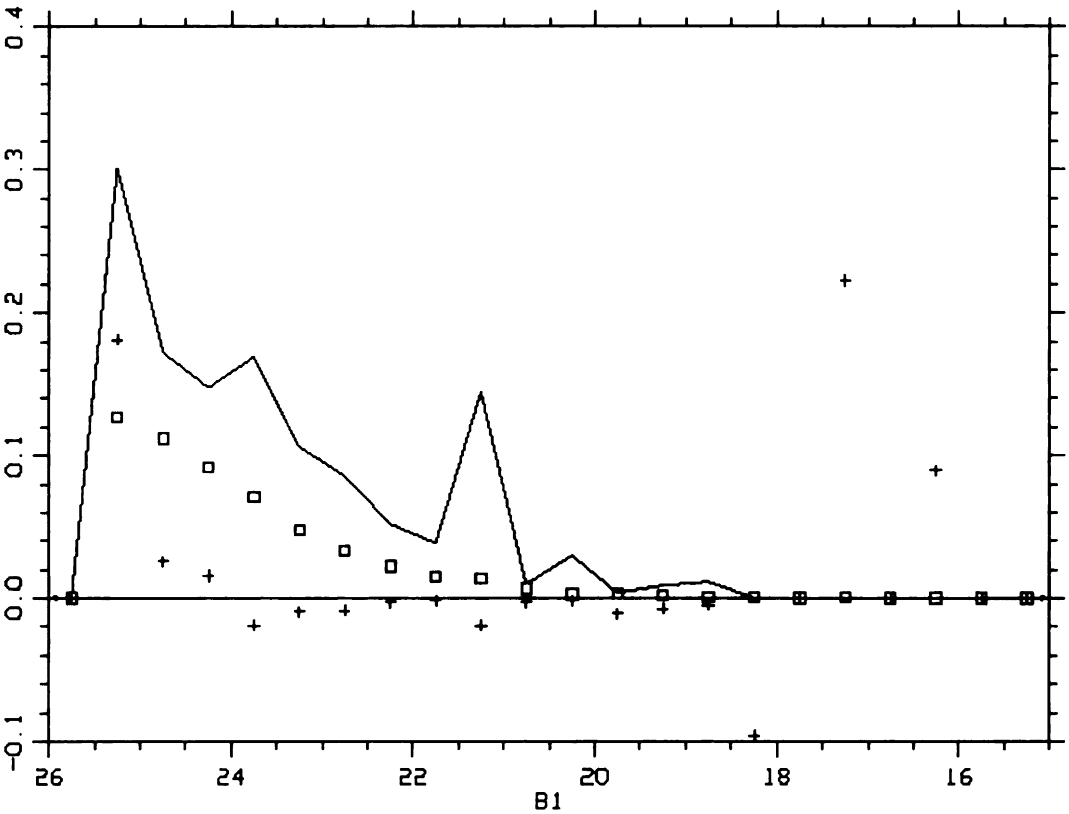

Figure 2.2: A comparison of photometry in DWF frame 1 and 2. The median of the magnitude difference between objects measured in DWF frame 1 and DWF frame 2 versus magnitude in frame 1. The crosses represent the median difference between the two frames, the boxes represent the median photometric uncertainty at that magnitude, and the line represents the dispersion of the median magnitude difference. The data are grouped in bins 0.5 magnitudes wide.

square size is used because the magnitude difference between two adjacent frames is smallest for a 32 $\times$ 32 background. The photometric errors of the objects are based on the local background found in each background square.

There is overlap between the frames of the DWF. Frame 1 is centered about right ascension 14^h26^m and declination $34°56'$, while frame 2 is centered about right ascension 14^h26^m and declination $35°56'$. There is roughly 1 arcminute of overlap between the two frames. This overlap region allows comparison of the photometry of the two frames.

The results of photometry performed on frame 1 are consistent with the results of photometry performed on frame 2. Figure 2.1 is a plot of the magnitude difference between objects in frame 1 and frame 2 of the DWF versus Bw magnitude of the first frame. The difference is centered around zero, so there is no consistent offset in magnitude between the two frames.

There is no bias between magnitudes measured for frame 1 and magnitudes measured for frame 2. Figure 2.2 is a plot of the median of the magnitude difference between frame 1 and frame 2, the median photometric uncertainty, and the dispersion of the median of the magnitude difference versus magnitude of frame 1. The median of the magnitude difference between frames is expected to remain near zero and stay smaller than the magnitude uncertainty. The median difference between magnitudes meets this expectation for magnitudes from $19 < B < 25$ where the bulk of the galaxies lie. The large median differences at $B < 18.5$ and $B > 25$ are due to small numbers of very bright or very faint galaxies present in both frames. Therefore, there is no bias present. Furthermore, the dispersion of the median of the magnitude difference is expected to be roughly $\sqrt{2}$ greater than the median uncertainty. The dispersion of the median of the magnitude difference meets this expectation. Therefore, there is no magnitude bias between these two frames of the DWF.

Pixels at the edge of the raw DWF frames were removed before performing photometry on all colors. This pruning was necessary to ensure that all frames were the same size. The Source Extractor (SExtractor) software package used here required that all images were the same size to perform detection in one image and photometry in another. The frames were pruned to 8192×8192 pixels to match the size of the detector. This size ensures that all objects present in one color will be present in the other two colors.

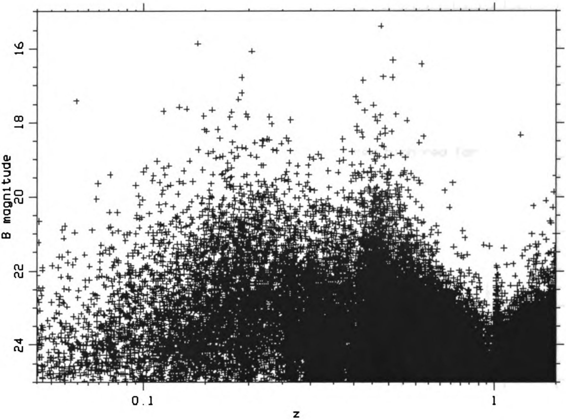

Figure 2.3: The Hubble diagram (magnitude vs. redshift) of all four pruned frames of the DWF. These redshifts were calculated with templates up to $z = 1.5$.

2.3 Redshifts

2.3.1 First Redshift Attempt

The photometric redshift technique of the Appendix was applied to the data set after the completion of photometry. The only difference in creating fiducial galaxies between the technique of the Appendix and this implementation is the use of the three DWF filters instead of the four HDF filters. Otherwise, the fiducials are created in the same manner as in the Appendix.

Stars and galaxies are separated based on their spectral energy distributions (SEDs). Objects that best matched a fiducial galaxy are classified as galaxies. Objects that best matched a fiducial star are classified as stars.

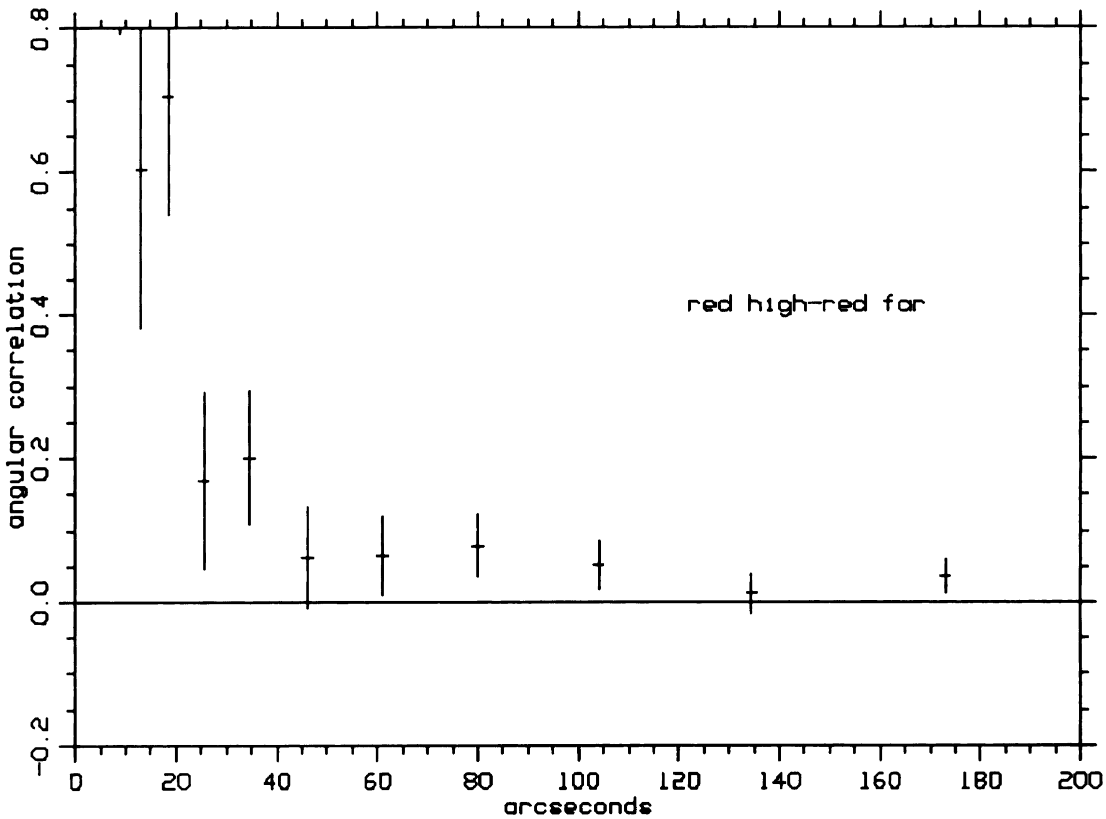

Figure 2.4: The angular correlation between galaxies at $z > 1$ and galaxies at $0.8 < z < 1$. The correlation is positive, indicating autocorrelation.

The first pass at calculating photometric redshifts used templates ranging from $z = 0.005$ to $z = 1.5$. The resulting redshifts were combined into one Hubble diagram (magnitude vs. redshift), shown in Figure 2.3. There is obviously an error for galaxies at $z_{\rm ph} > 1$, as the flux of objects should not increase with increasing distance.

The angular correlation of galaxies at high redshift ($z_{\rm ph} > 1$) and lower redshift galaxies ($z_{\rm ph} < 1$) was measured to determine if the galaxies that were assigned high photometric redshifts were really misclassified galaxies with lower redshifts. The autocorrelation of galaxies as a function of angular separation θ follows the functional form $\theta^{-0.8}$ due to clustering. Therefore, if the angular correlation between galaxies with high photometric redshift and lower photometric redshift is positive, then the high redshift galaxies are really misclassified lower redshift galaxies.

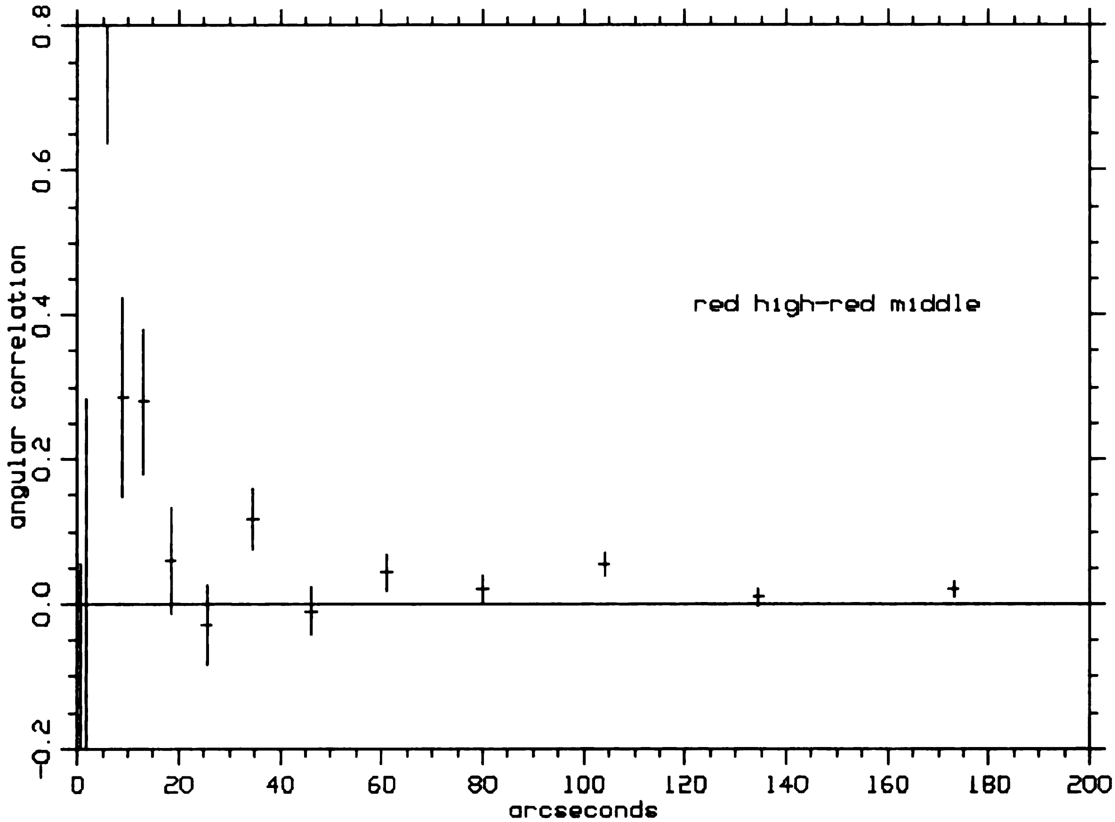

Figure 2.5: The angular correlation between galaxies at $z > 1$ and galaxies at $0.6 < z < 0.8$. The correlation is again positive, indicating autocorrelation.

The galaxies assigned a high photometric redshift are misclassified lower redshift galaxies. Figure 2.4 is a plot of angular correlation between galaxies with $z_{\text{ph}} > 1$ and galaxies with $0.8 < z_{\text{ph}} < 1$. Figure 2.5 is a plot of angular correlation between galaxies with $z_{\text{ph}} > 1$ and galaxies with $0.6 < z_{\text{ph}} < 0.8$. Both show clear positive correlation between the high and low redshift galaxies, indicating that most of the galaxies assigned a redshift greater than 1 are probably lower redshift galaxies. Therefore, templates with redshifts above 1 should be removed from the template set.

2.3.2 Second Redshift Attempt

The solution to misclassified high redshift galaxies is to recalculate photometric redshifts with fiducials limited to a maximum of $z = 1$. This limit was chosen because

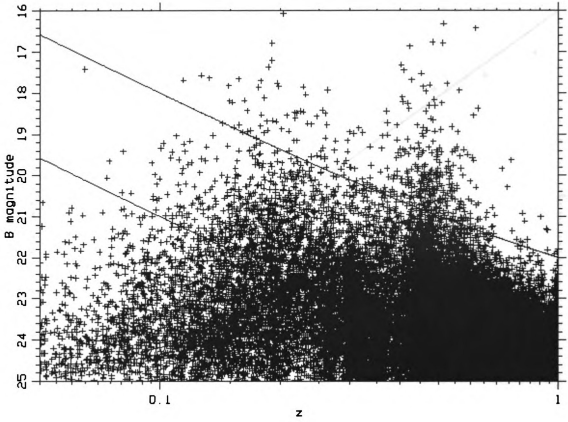

Figure 2.6: The Hubble diagram (magnitude vs. redshift) of all four pruned frames of the DWF. The lines represent constant luminosity so that Bw = 25 and Bw = 22 at z=1.

it is the maximum redshift at which the 4000 Å break may be detected in the I-band. Figure 2.6 is the Hubble diagram for 57,685 galaxies brighter than $B = 25$ between $z = 0.05$ and $z = 1.0$. The brightest objects near $z = 0.5$ are probably misclassified stars because galaxies at that distance are not that bright. The number of galaxies at each redshift appears to increase with redshift and, aside from a few outliers, the maximum magnitude of the galaxies decreases with redshift.

The rate of change of the number of galaxies as a function of redshift in the DWF increases with redshift. The galaxies were separated into redshift bins. The galaxies in each bin were counted down to a magnitude limit determined by the redshift of the bin. The greater the redshift, the fainter the magnitude limit by the distance modulus

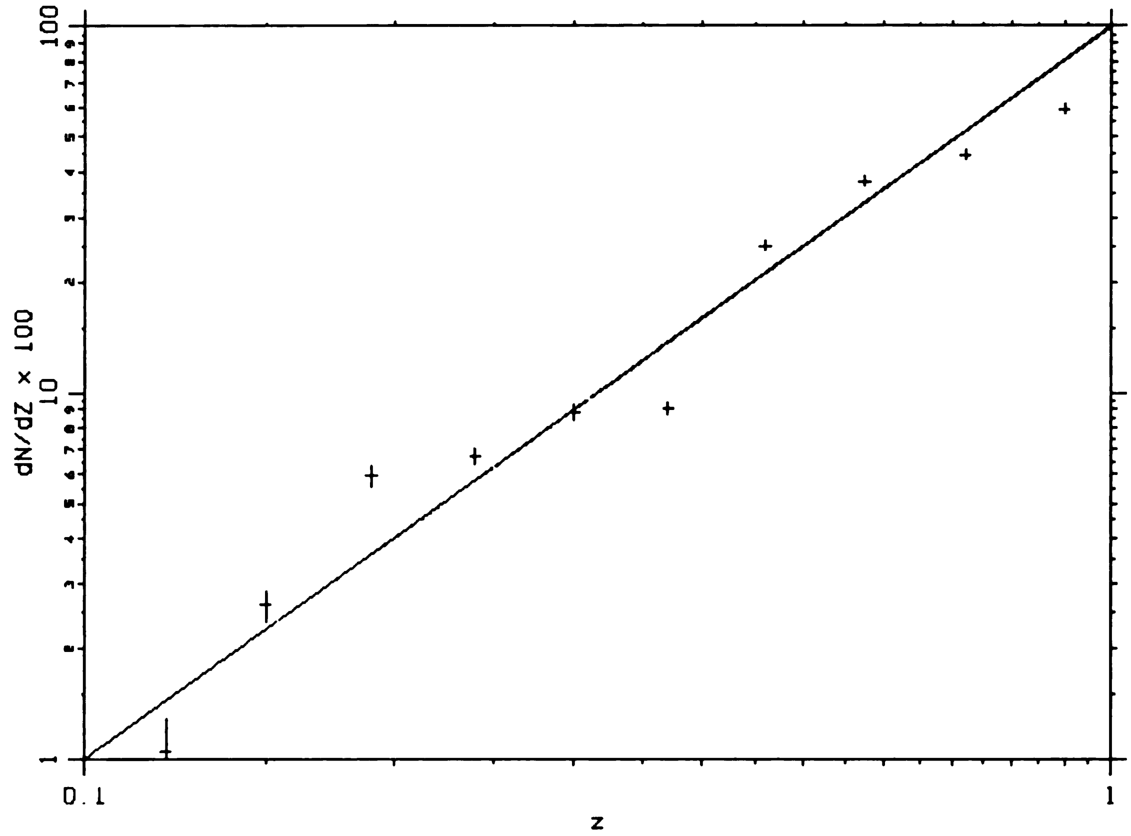

Figure 2.7: The rate of change of number of galaxies versus redshift in the DWF. The line represents $\frac{dN}{dz} \propto z^2$.

$(-5 \log distance)$. One expects the number of galaxies in each bin to increase as the square of redshift since redshift is approximately equal to distance. Figure 2.7 is a plot of $\frac{dN}{dz}$ versus redshift. The line represents $\frac{dN}{dz} \propto z^2$. There appear to be too few galaxies at $z > 0.7$. The low count is probably due to the lack of k-correction or luminosity evolution in the determination of the magnitude limits. The apparent deficit at $z = 0.35$ could be due to the 4000 Å break redshifted between the Bw and R filters at redshifts between $z = 0.23$ and $z = 0.38$. There is a gap of 60 nm between the Bw- and R-band filters. While the data do not fit the model, the rate of change of galaxies with respect to redshift does increase at a rate close to that predicted by the model.

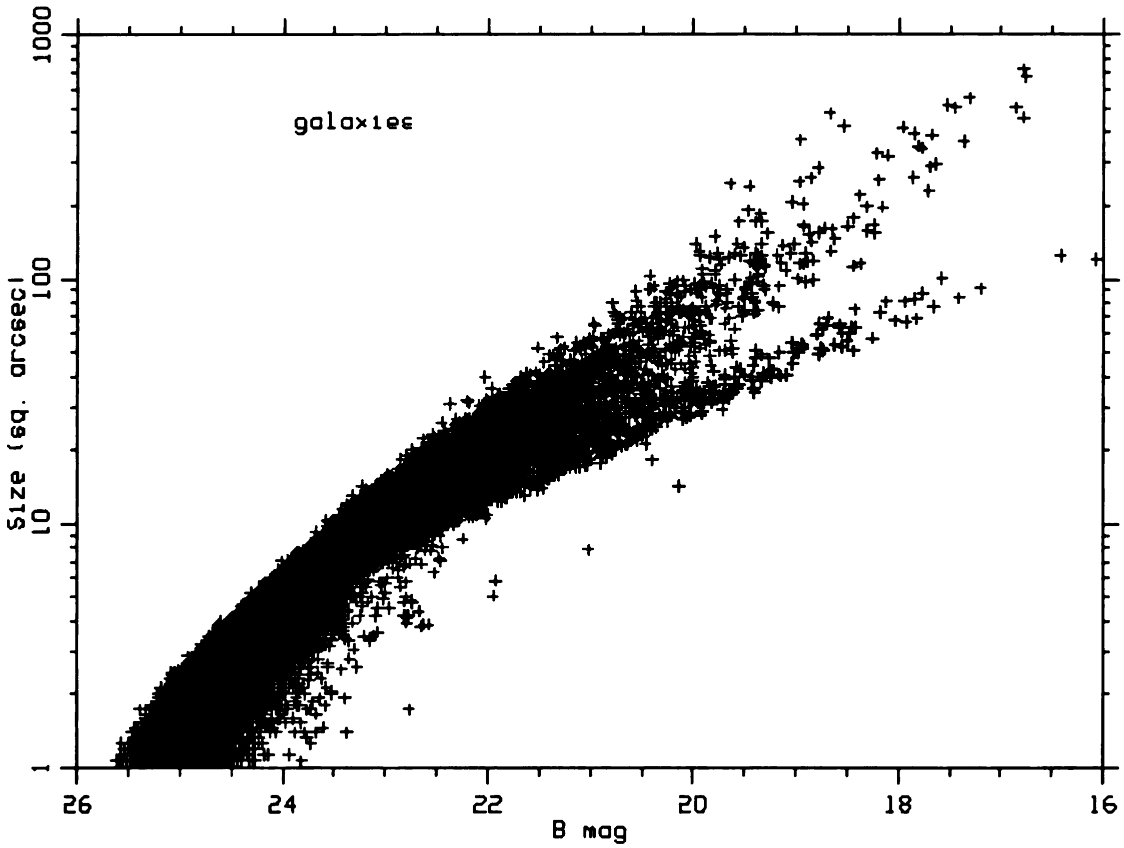

Figure 2.8: Isophotal area of galaxies versus redshift in the DWF.

The angular size of the galaxies increases as flux increases. This result is expected because brighter galaxies will tend to be closer than far galaxies, so the brighter galaxies should appear bigger than fainter galaxies. Figure 2.8 is a plot of the isophotal size of galaxies versus magnitude. The isophotal size is the number of pixels within a given isophote. In this case, the isophotal size is everything 1.9σ above the local background. There is a smaller range in the size of dim things because the galaxies approximate point sources at large magnitudes.

The angular size of the stars also increases as flux increases. The size is expected to increase with flux because the point spread function of stars is approximately gaussian. For a typical DWF value of 1.3 arcsecond seeing, the point spread function is $exp(-0.41 \times r^2)$, where r is radius in arcseconds. As brightness increases, a larger

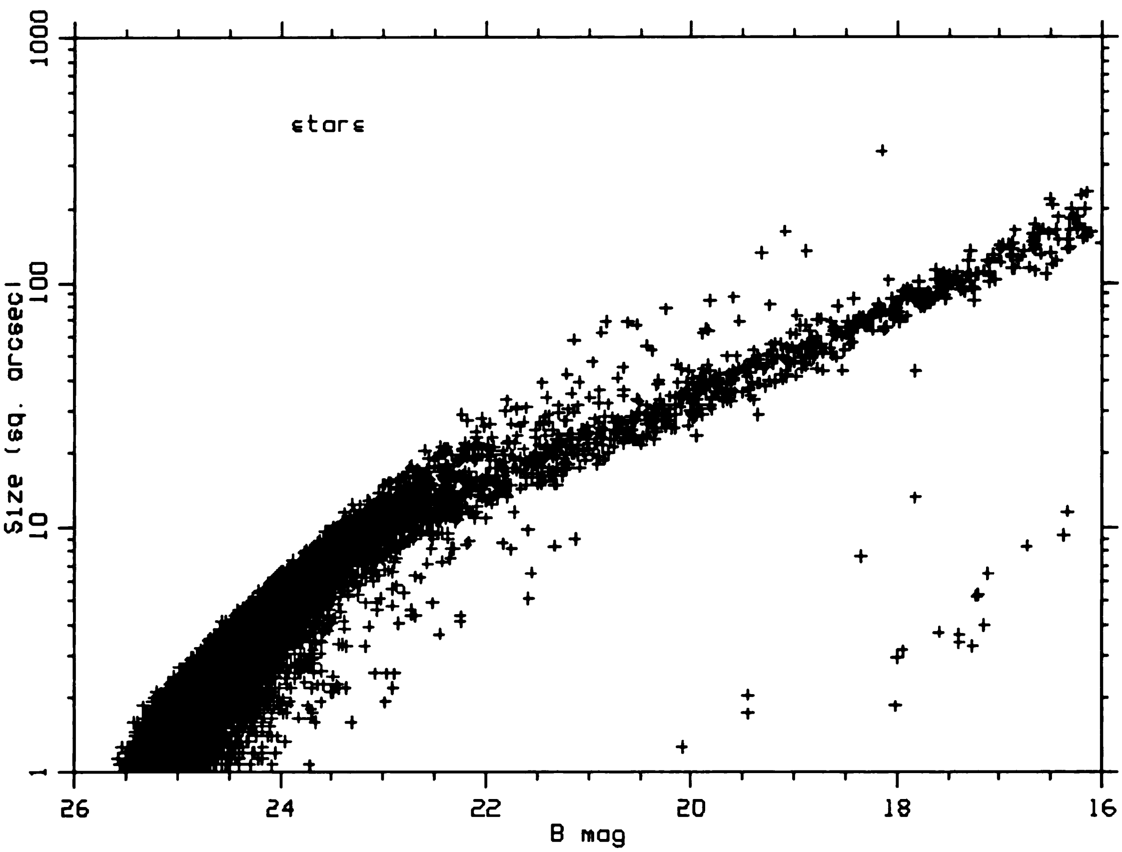

Figure 2.9: Isophotal area of stars versus redshift in the DWF.

area of the point spread function is brighter than the background level. Therefore, the brighter stars appear bigger than smaller stars. Figure 2.9 is a plot of the isophotal size of stars versus magnitude. There is a small range in the size of both bright and faint objects because the stars are point sources, not extended objects. The fact that the sub-images that contributed to this sample had different seeing also contributes to the size range of the bright stars. The bright objects ($B\mathrm{w} < 20$) that are smaller than the main grouping (< 20 arcseconds) have been confirmed to be false detections by visually inspecting the images. These objects have been removed from the catalog.

The size-magnitude plots show a distinction between stars and galaxies at magnitudes brighter than 22. The slope of the size-magnitude relation for stars is much flatter than the slope of the size-magnitude relation for galaxies. The slope is flatter

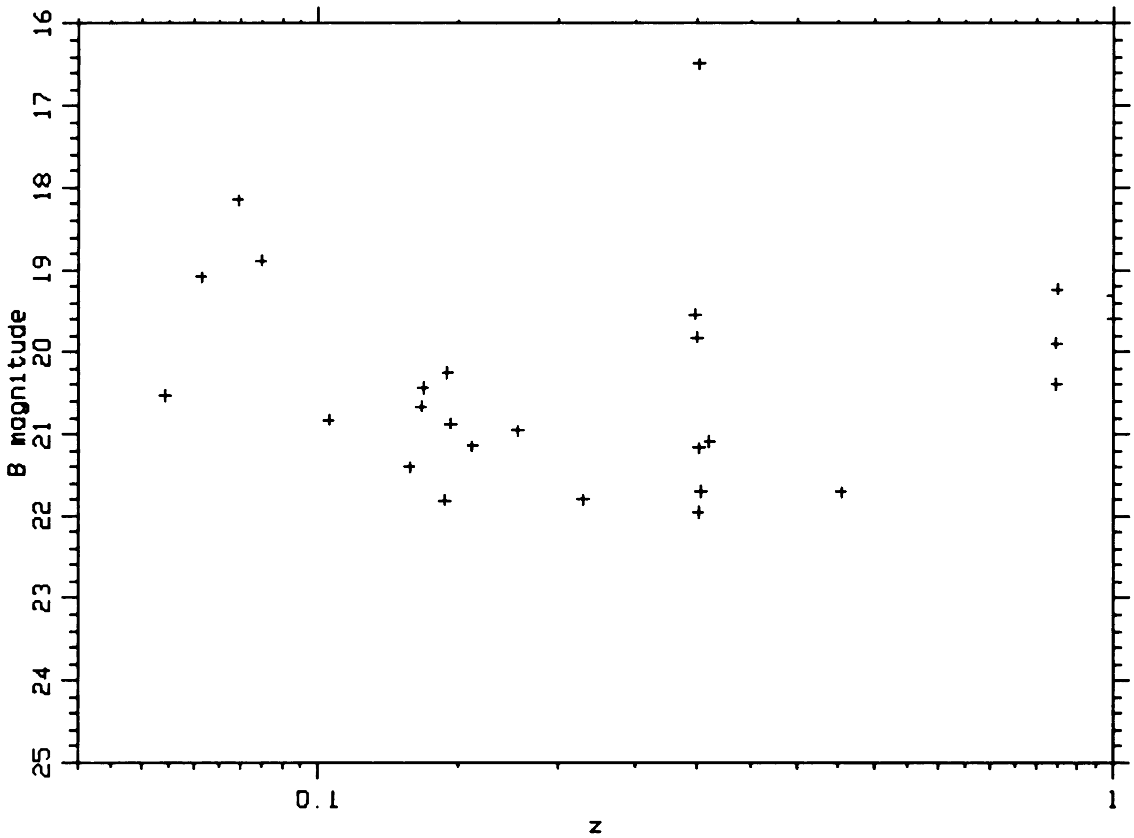

Figure 2.10: The Hubble diagram of the large bright objects identified as stars in the DWF.

because stars are point sources, while galaxies are extended objects. A few objects classified as stars follow the size-magnitude relation for galaxies and vice-versa. These objects are potentially misclassified.

A Hubble diagram of the large stars shows some confusion between bright stars and low-redshift galaxies. Figure 2.10 is the Hubble diagram of the bright stars that are larger than most stars of similar magnitude. The redshifts are assigned to the stars as if the stars were really galaxies. A number of the bright stars assigned low redshifts are indistinguishable from bright, low-redshift galaxies. Therefore, the objects classified as stars that are larger than most stars are probably misclassified galaxies.

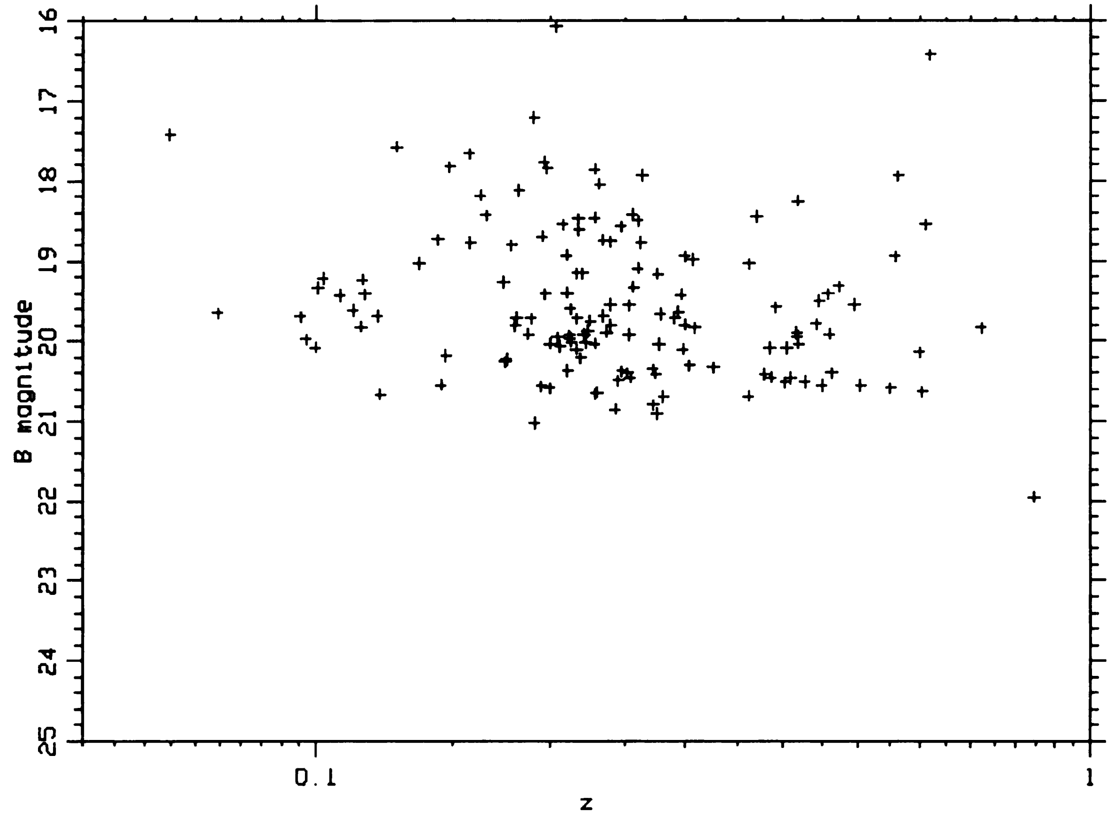

Figure 2.11: The Hubble diagram of the small bright objects identified as galaxies in the DWF.

A Hubble diagram of the small galaxies shows some confusion between bright stars and galaxies. Figure 2.11 is the Hubble diagram of the bright galaxies that are smaller than most galaxies of similar magnitude. The brightest objects in this diagram are probably stars, because galaxies cannot be as bright as those objects at high magnitude. The fainter objects are not as distinguishable, but are not inconsistent with classification as galaxies. Therefore, while the brightest objects are surely stars, the fainter ones could be stars or galaxies.

A Hubble diagram of the remaining objects classified as stars shows a distinction between stars and galaxies. Figure 2.12 is the Hubble diagram of both small bright objects and faint objects classified as stars. The stars are again assigned redshifts as if they were galaxies There is a large population of faint objects assigned a redshift

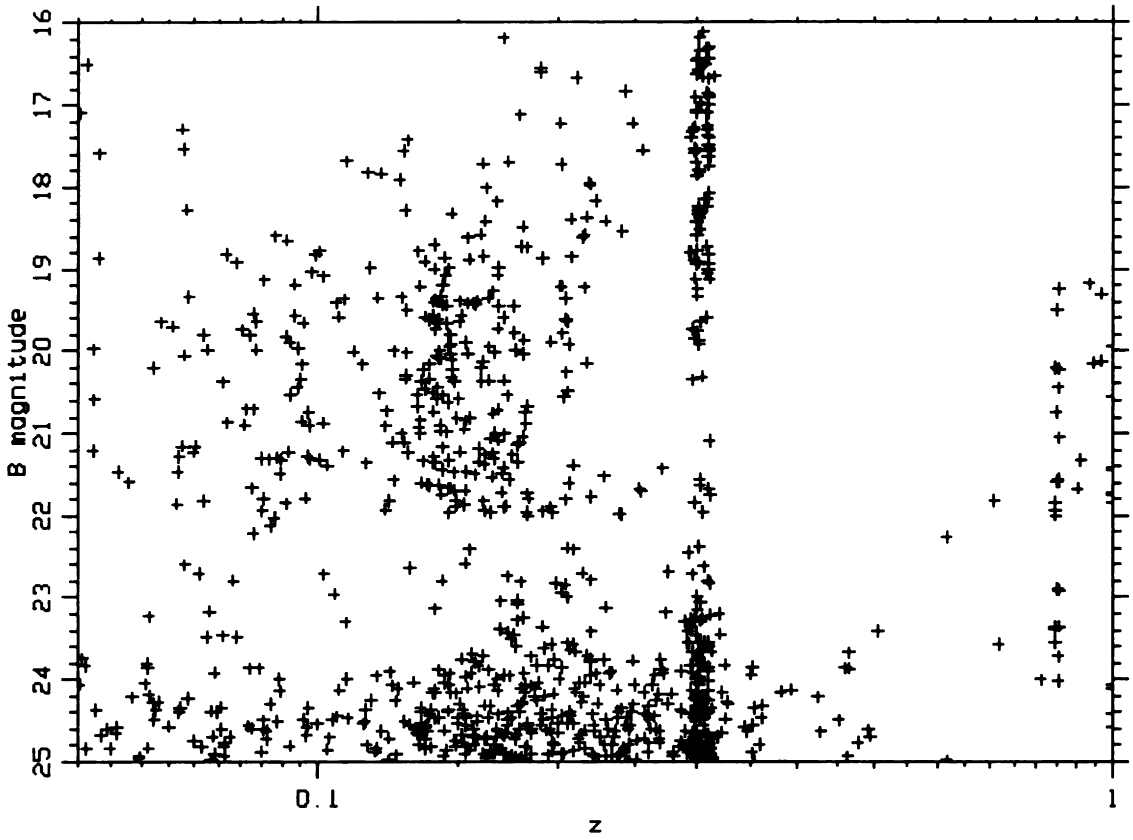

Figure 2.12: The Hubble diagram of faint and small bright objects identifed as stars. One out of every 10 objects fainter than 22^{nd} magnitude are plotted.

less than 0.3. These objects are stars because there is not a large population of faint nearby galaxies. Therefore, most of the objects classified as stars are truly stars.

2.4 Catalogues

Catalogues of stars and galaxies found in the DWF have been assembled and posted for public use. Table 2.1 gives the position, fluxes, size, and ellipticity, for a small sample of the objects in the DWF. Right ascensions are given as arcseconds with an offset of 14 hours, 24 minutes. Declinations are given as arcseconds with an offset of 34 degrees. The positions come from the SExtractor output, which derives the positions from the position solution put in the FITS header by Jannuzi and Dey.

N	X	Y	RA	Dec	$Flux_B$	$\delta Flux_B$	$Flux_R$	$\delta Flux_R$	$Flux_I$	$\delta Flux_I$	Size	πAB	Ellip.
1	3314	3	2085.6	2339.1	0.00751	5.69E-04	0.00397	0.00294	0.0148	0.00131	0.5	1.0	0.204
2	4225	3	1799.9	2335.5	0.00905	7.08E-04	0.0141	0.00366	0.0132	0.00163	1.3	1.2	0.074
3	4524	3	1706.4	2334.4	0.0141	8.83E-04	0.0461	0.00457	0.0481	0.00204	1.7	1.7	0.226
4	5890	3	1278.1	2328.7	0.0343	0.00142	0.0708	0.00736	0.110	0.00328	3.5	3.3	0.617
5	5855	5	1289.1	2329.4	0.0109	8.26E-04	0.0210	0.00427	0.0277	0.00190	1.3	1.4	0.155
6	2990	3	2187.0	2340.3	0.0202	8.84E-04	0.0213	0.00457	0.0382	0.00204	3.0	2.4	0.354
7	939	4	2830.1	2347.3	0.0273	9.87E-04	0.0539	0.00510	0.0722	0.00227	5.1	3.1	0.453
8	2894	6	2217.0	2341.4	0.0130	9.28E-04	0.0225	0.00480	0.0277	0.00214	1.9	1.6	0.116
9	6836	12	981.8	2326.8	0.0120	9.79E-04	0.0215	0.00507	0.0135	0.00226	0.9	1.0	0.003
10	4073	13	1847.5	2338.9	0.0125	9.05E-04	0.0213	0.00468	0.0254	0.00209	0.7	1.0	0.133
11	278	4	3037.3	2349.5	0.0169	7.39E-04	0.0576	0.00383	0.233	0.00171	3.5	2.0	0.006
12	7524	9	766.1	2323.2	0.0151	9.52E-04	0.0372	0.00493	0.0440	0.00219	2.3	1.7	0.116
13	5275	12	1471.0	2333.7	0.0120	9.72E-04	0.0169	0.00503	0.0108	0.00224	1.1	1.2	0.008
14	2325	13	2395.5	2345.2	0.0106	8.93E-04	0.0273	0.00463	0.0436	0.00206	1.5	1.3	0.009
15	146	15	3078.8	2352.8	0.0104	8.32E-04	0.0202	0.00430	0.0302	0.00192	0.9	1.1	0.117

Table 2.1: A partial list of objects found in the Deep Wide Field. "N" is short for "Number." "Size" is short for the size in pixels of the isophote 1.9σ above background. The elliptical size (πAB) is in pixels. "X" and "Y" positions are also in pixels. Right ascension and declination are in arcseconds with respect to 14 hours 24 minutes and 34 degrees, respectively. Fluxes are normalized so that 1 count is 20^{th} AB magnitude. The complete table may be found at `http://www.pa.msu.edu/~davism/DWFphot.txt`.

Number	z	δz	Type	χ^2	NB Type	NB z	NB χ^2
1	1.00	0.15	C10	4	C22	0.00	15
2	0.00	0.10	F4V	0.2	C10	0.00	0.4
3	0.31	0.14	G6V	1	C36	0.30	1
4	0.68	0.10	C27	0.2	C56	0.10	1
5	0.02	0.81	C54	0.3	C56	0.01	0.3
6	0.00	0.11	C22	4	BD17	0.00	22
7	0.63	0.64	C10	0.3	C57	0.02	0.4
8	0.01	0.21	C38	0.2	C35	0.03	0.2
9	0.00	0.07	A5V	2	C10	0.00	12
10	0.12	0.20	C15	0.2	C19	0.10	0.3
11	1.00	0.01	C88	32	C87	0.96	77
12	0.19	0.44	G8V	0.2	C37	0.19	0.2
13	0.00	0.06	A5V	0.7	C10	0.00	8
14	0.64	0.20	C45	0.2	C67	0.13	0.8
15	0.68	0.70	C20	0.2	C60	0.04	0.4

Table 2.2: A partial table of redshift, object type, χ^2 of the fit, next best object, next best redshift, and χ^2 of the fit of the next best object. The number refers to the object number in the photometry table. The complete data may be found at `http://www.pa.msu.edu/~davism/DWFz.txt`.

The position solution is accurate to 0.5 arcseconds, so it is reasonable to assume the positions of the catalog have a similar accuracy [18]. Table 2.2 gives the redshift, object type, χ^2, and second best fit object type, redshift, and χ^2 for a small sample of the galaxies found in the DWF. The galaxy types are indicated by rest frame B-V color. A "C95" has a B-V color of 0.95, a "C90" is 0.90, and so forth. The star types are not intended to be accurate stellar classifications, but to label that the object (or second best type) is a star. Likewise, the redshift listed for the stars is the redshift as if they were galaxies. The complete tables may be found online as noted in the captions of the sample tables. After pruning the original frames to 8192×8192 pixels, there are 37 objects that are present in two frames and are double counted. These objects have not been removed from the catalog.

2.5 Conclusion

The data from the Deep Wide Field are ready for further study and public release. The Hubble diagram shows that the galaxies get fainter with redshift. The rate of change of galaxy counts increases with redshift. Bright stars are smaller than bright galaxies. Galaxies and stars are separated fairly well for $Bw < 22$.

Chapter 3

Galaxy-Galaxy Lensing in the Deep Wide Field

3.1 Method

Galaxy-galaxy lensing depletion is the gravitational deflection of the position of background galaxies in an area surrounding foreground galaxies. The mathematics of lensing depletion are discussed in Chapter 1. This chapter takes the photometric redshift data from Chapter 2, finds the lensing depletion signals from four galaxy sets at two different redshifts, and then calculates the rotation velocity of these galaxies.

The choice of cosmology affects the calculated rotation velocity. While recent observations conclude that the "proper" cosmology is dark energy dominated with $\Omega_m = 0.3$ and $\Omega_\Lambda = 0.7$, Wilson *et al.* show either a dark energy cosmology or Einstein-deSitter has little effect on lensing results at low redshift [30]. However, for the sake of completeness, both cosmologies are used to calculate rotation velocities. The luminosity distance d is given by:

$$\frac{1}{H_0}\int_0^z ((1+x)^2(1+\Omega_m x) - x(2+x)\Omega_\Lambda)^{-0.5}dx \tag{3.1}$$

This distance reduces to $\frac{2}{H_0}(1 - \frac{1}{\sqrt{1+z}})$ for an Einstein-deSitter cosmology, but must be evaluated numerically for a dark energy dominated cosmology. Then, depletion curves as given in Eq. 1.1 are fit to the data to determine r, the angular size of the Einstein radius. The corresponding linear size is given by $R_{\mathrm{E}} = r \times D_{\mathrm{OL}} \times (1 + z_{\mathrm{lens}})^{-2} \times (206265)^{-1}$. Substituting into Equation 1.5 gives:

$$v = \frac{c}{1 + z_{\mathrm{lens}}} \sqrt{\frac{r D_{\mathrm{OS}}}{206265 \times 4\pi D_{\mathrm{LS}}}} \tag{3.2}$$

The appropriate values of D_{OS} and D_{LS} are substituted depending on the cosmology, the median redshift of the foreground galaxies, and the median redshift of the background galaxies. The Hubble constant cancels out of the rotation velocity calculation, so the value of H_0 has no effect on the rotation velocity. However, the value of H_0 will determine the projected size of the lens. A value of (100 km/s/Mpc) is assumed.

3.2 Lensing Data

3.2.1 Considerations

Two sets of foreground and background galaxies are selected so that galaxy rotation velocity could be measured at two different redshifts. The first foreground set runs from $z = 0.1$ to $z = 0.3$ with a median of $z = 0.2$. The magnitude cutoff is $B < 23$, 2 magnitudes below $m^* = 21$ for galaxies from $z = 0.1$ to $z = 0.3$. The second foreground set runs from $z = 0.4$ to $z = 0.6$ with a median of $z = 0.5$. The magnitude cutoff for the second foreground set is $B < 25$, 2 magnitudes below $m^* = 23$ for galaxies from $z = 0.4$ to $z = 0.6$. This cutoff is different because $z = 0.5$ is roughly 2.5 times as distant as $z = 0.2$. That distance translates to a flux reduction of 2 magnitudes. The first background set consists of all galaxies with $z > 0.6$ with a median of $z = 0.8$. The second background set consists of all galaxies with

$z > 0.9$ with a median of $z = 0.96$. The first foreground set is paired with the first background set and the second foreground set is paired with the second background set.

The width and redshift of the galaxy bins are selected so the median redshift errors for each bin do not cause overlap. The median redshift error at $z = 0.3$ (the high edge of the first foreground bin) is 0.16, while the median redshift error at $z = 0.6$ (the low edge of the first background bin) is 0.13. Therefore, there should be no overlap between the first set of foreground and background galaxies. The median redshift error at $z = 0.9$ (the low edge of the second background bin) is 0.16. Given the redshift error of 0.13 at $z = 0.6$ (the high edge of the second foreground bin) and the redshift error at $z = 0.9$, there should be no overlap between the second set of foreground and background galaxies.

Each set of foreground galaxies is further separated into red and blue galaxies. Everything with a rest-frame $B-V$ greater than or equal to 0.61 is considered red, and everything with a rest-frame $B-V$ less than 0.61 is considered blue. For reference, red S0 galaxies have a $B-V$ color around 0.95, while blue Im galaxies have a $B-V$ color around 0.3.

The number of galaxies in the background sample determines the background magnification constant α (Eq. 1.2). The log of the number of background galaxies with $B\mathrm{w} < 24.9$ is subtracted from the log of the number of galaxies with $B\mathrm{w} < 25.1$. The difference is divided by 0.2 to calculate $\frac{d \log N}{dm}$. For the background sample $0.6 \leq z \leq 1.0$ there were 26375 galaxies down to $B\mathrm{w} = 25.1$ and 23283 galaxies down to $Bw = 24.9$. These numbers give $\alpha = 0.27 \pm 0.02$ assuming errors go as $\sqrt{N}$. For the background sample $0.9 \leq z \leq 1.0$ there were 9083 galaxies down to $B\mathrm{w} = 25.1$ and 7654 galaxies down to $B\mathrm{w} = 24.9$. These numbers give $\alpha = 0.37 \pm 0.03$.

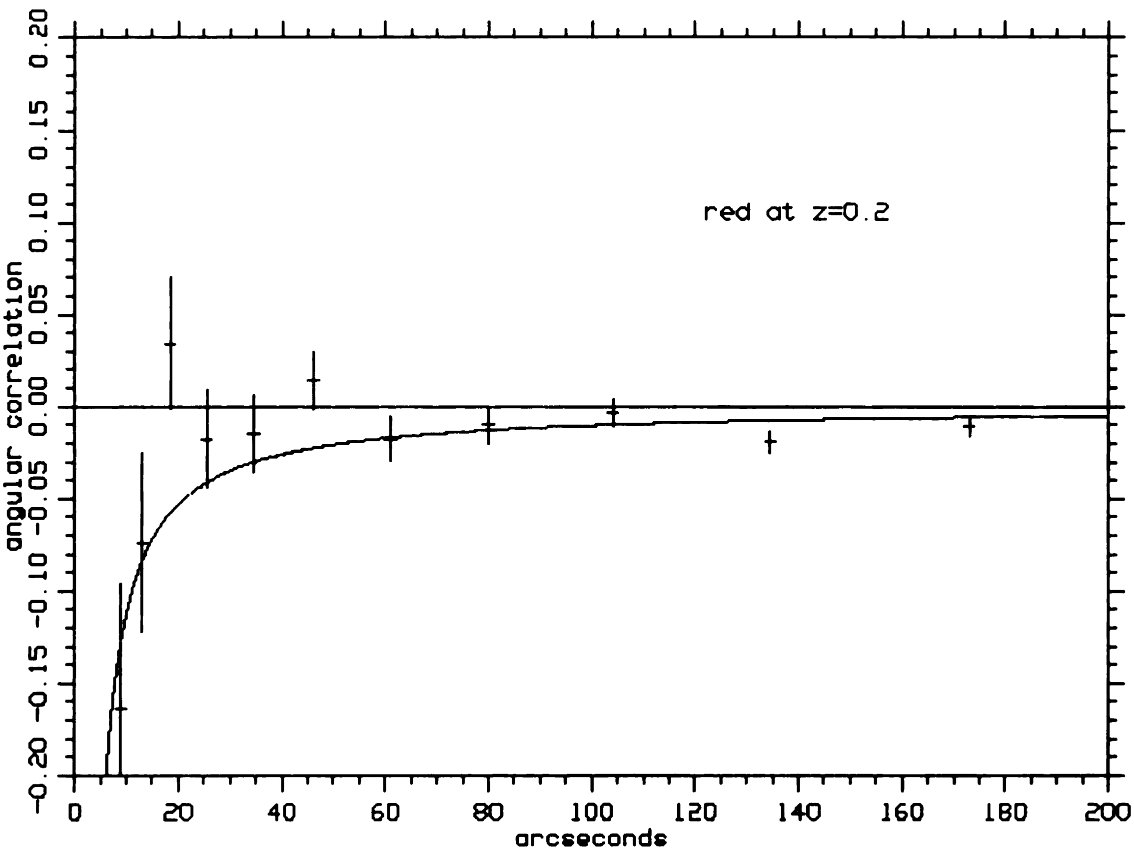

Figure 3.1: The angular correlation of red foreground galaxies with background galaxies. The background sample is $z > 0.6$. The foreground sample is $0.1 < z < 0.3$.

3.2.2 Results

The first angular correlation measurement is between red galaxies between $z = 0.1$ and $z = 0.3$ and background galaxies between $z = 0.6$ and $z = 1.0$. Figure 3.1 is a plot of the angular correlation between these two samples. There is clearly a depletion in the number of background galaxies at radii less than 60 arcseconds, or 100 kpc at $z = 0.2$. The Einstein radius of the best fit curve is $r = 2.6 \pm 0.6$ arcseconds. The reduced χ^2 of the fit is 1.8.

The second angular correlation measurement is between blue galaxies between $z = 0.1$ and $z = 0.3$ and background galaxies between $z = 0.6$ and $z = 1.0$. Figure 3.2 is a plot of angular correlation between these two samples. There is again a depletion

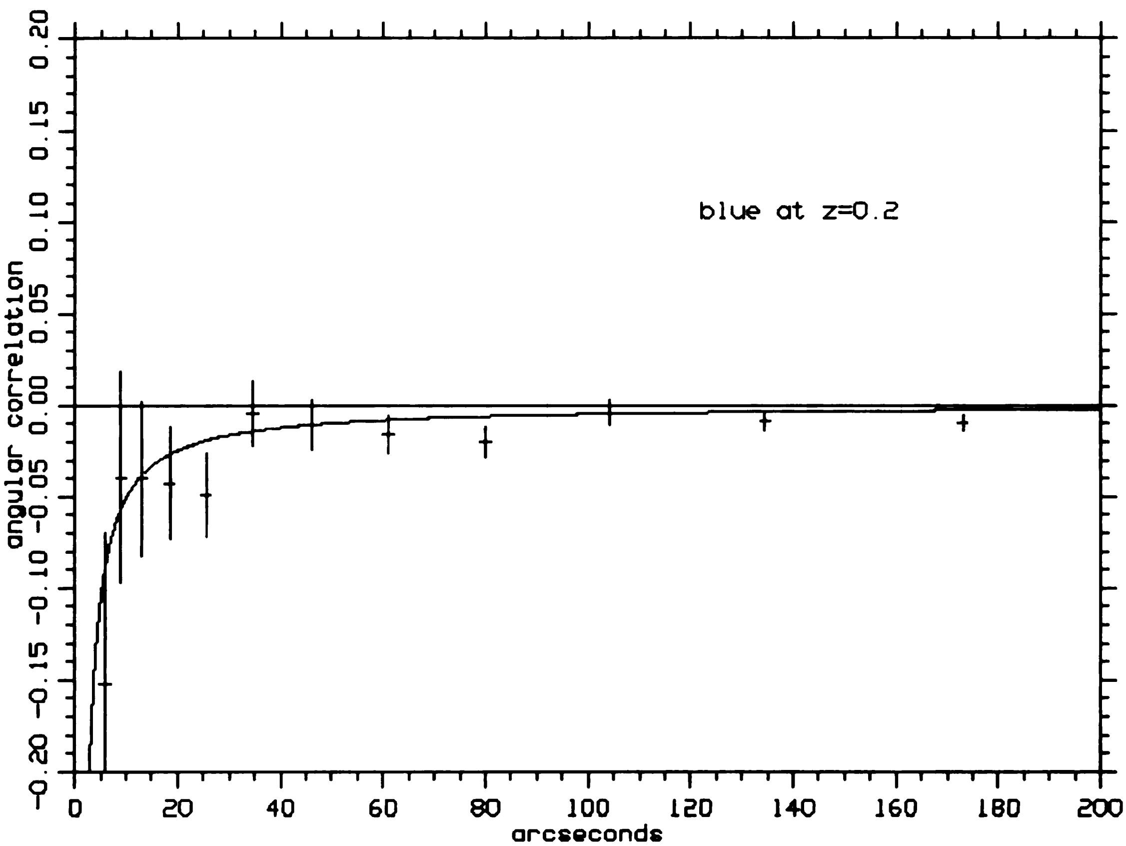

Figure 3.2: The angular correlation of blue foreground galaxies with background galaxies. The background sample is $z > 0.6$. The foreground sample is $0.1 < z < 0.3$.

in the number of background galaxies at radii less than 60 arcseconds, or 100 kpc at $z = 0.2$. The Einstein radius of the best fit curve is $r = 1.4 \pm 0.2$ arcseconds. The reduced χ^2 of the fit is 0.89.

The third angular correlation measurement is between red galaxies between $z = 0.4$ and $z = 0.6$ and background galaxies between $z = 0.9$ and $z = 1.0$. Figure 3.3 is a plot of the angular correlation between these two samples. There is clearly a depletion in the number of background galaxies at radii less than 80 arcseconds, or 190 kpc at $z = 0.5$. The Einstein radius of the best fit curve is $r = 2.7 \pm 0.5$ arcseconds. The reduced χ^2 of the fit is 1.9.

The final angular correlation measurement is between blue galaxies between $z = 0.4$ and $z = 0.6$ and background galaxies between $z = 0.9$ and $z = 1.0$. Figure 3.4

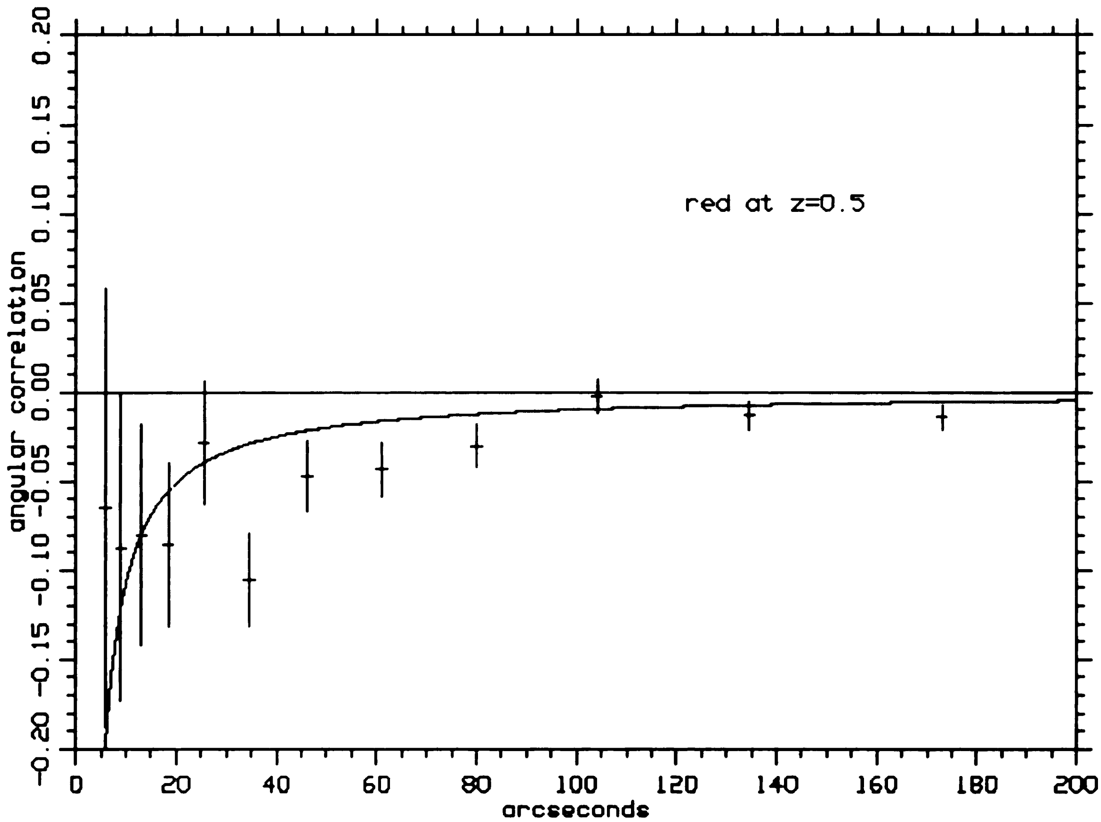

Figure 3.3: The angular correlation of red foreground galaxies with background galaxies. The background sample is $z > 0.9$. The foreground sample is $0.4 < z < 0.6$.

is a plot of the angular correlation between these two samples. There is a depletion in the number of background galaxies at radii less than 60 arcseconds, or 140 kpc at $z = 0.5$. However, this depletion is the noisiest of the four. The Einstein radius of the best fit curve is $r = 1.1 \pm 0.6$ arcseconds. The reduced χ^2 of the fit is 2.0.

3.2.3 Comparison

The sample of foreground galaxies selected by this work is larger than the sample of foreground galaxies selected by Wilson *et al.* [30]. Figure 3.5 is a color-magnitude plot of the range of foreground galaxies selected by Wilson *et al.* and this work. The rest-frame color of Wilson's foreground galaxies is estimated from their measured

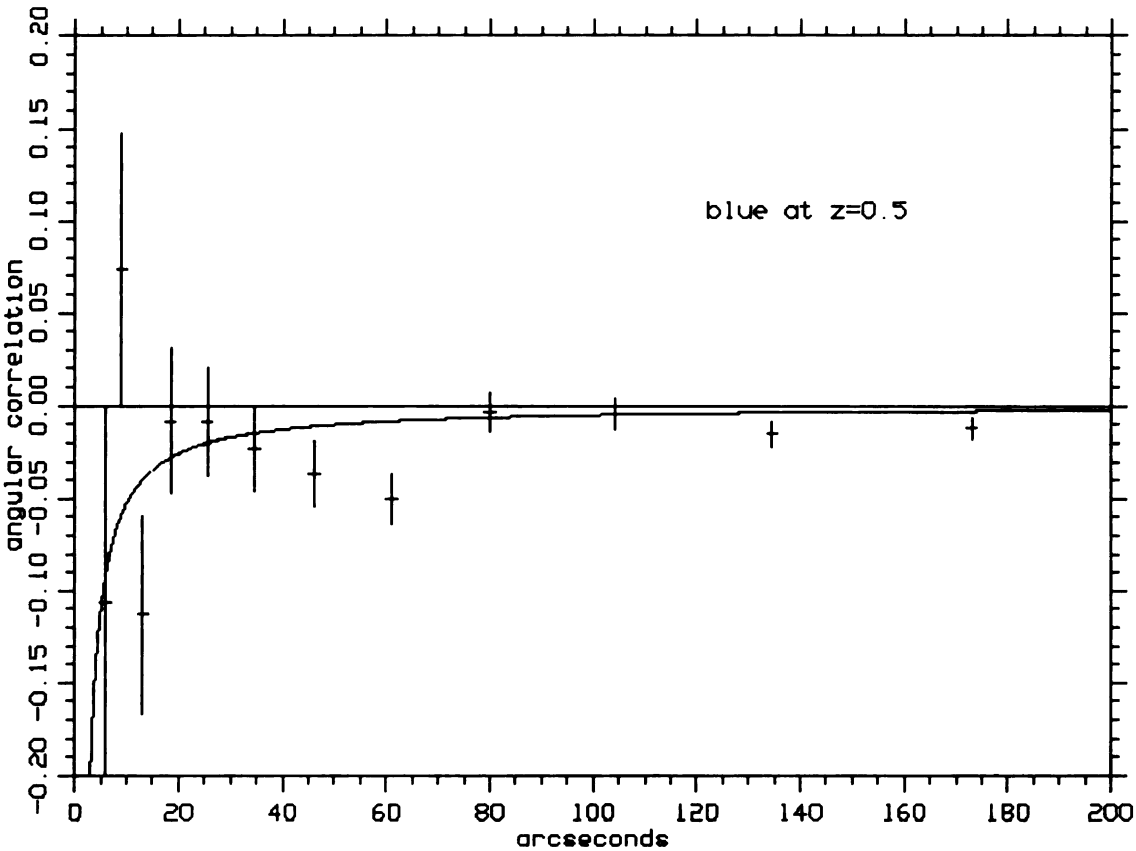

Figure 3.4: The angular correlation of blue foreground galaxies with background galaxies. The background sample is $z > 0.9$. The foreground sample is $0.4 < z < 0.6$.

color and estimated redshift. The magnitude of Wilson's foreground galaxies is taken as if they were at $z = 0.2$. The rest-frame color of the foreground galaxies of this work is taken from Figure A.2. The large rectangular area represents the colors and magnitudes of the foreground galaxies selected between $z = 0.1$ and $z = 0.3$.

The rotation velocity calculated for the red galaxies at $z = 0.2$ is 308^{+32}_{-35} km/s for an Einstein-deSitter cosmology and 297^{+31}_{-34} km/s for a dark energy cosmology. Wilson *et al.* measured a rotation velocity of 275^{+42}_{-50} km/s for an Einstein-deSitter cosmology and 255^{+36}_{-42} km/s for a dark energy cosmology for bright elliptical galaxies at $z = 0.2$ [30].

As shown in Figure 3.5, Wilson's foreground galaxy sample covers a smaller range of magnitudes and galaxy types than the foreground galaxy sample in Figure 3.1

color	z_f	z_b	R_E (arcsec)	reduced χ^2	$v(\Omega_m = 1)$ (km/s)	$v(\Omega_\Lambda = 0.7)$ (km/s)
red	0.20	0.76	2.6 ± 0.6	1.8	308^{+32}_{-35}	297^{+31}_{-34}
blue	0.21	0.76	1.4 ± 0.2	0.89	226^{+19}_{-20}	218^{+19}_{-20}
red	0.51	0.98	2.7 ± 0.5	1.9	342^{+29}_{-32}	319^{+27}_{-30}
blue	0.51	0.98	1.1 ± 0.6	2.0	216^{+49}_{-64}	201^{+46}_{-59}

Table 3.1: A table of foreground redshift, background redshift, Einstein radius, reduced χ^2, and rotation velocity for four foreground samples from the Deep Wide Field. The reduced χ^2 is calculated with 11 degrees of freedom.

because they were selected with two color photometry. Wilson also did not have photometric redshifts to determine the redshift of the background sample, unlike this background sample [30]. Instead, the redshifts of the background galaxies were estimated by comparing their flux with the luminosity function. Therefore, despite two different methods of measurement, the two results agree.

The rotation velocity calculated for the blue galaxies at $z = 0.2$ is 226^{+19}_{-20} km/s for an Einstein-deSitter cosmology and 218^{+19}_{-20} km/s for a dark energy cosmology. These values are clearly distinct from the rotation velocities for the red galaxies at the same redshift. Wilson *et al.* could not calculate the rotation velocity of blue galaxies due to their selection method [30].

The rotation velocity calculated for the red galaxies at $z = 0.5$ is 342^{+29}_{-32} km/s for an Einstein-deSitter cosmology and 319^{+27}_{-30} for a dark energy cosmology. While the two values agree, the choice of cosmology has a larger effect on the result at $z = 0.5$ than at $z = 0.2$.

Wilson *et al.* measured a rotation velocity of 285^{+38}_{-44} for an Einstein-deSitter cosmology and 253^{+30}_{-35} for a dark energy cosmology for bright elliptical galaxies at $z = 0.5$ [30]. Again, Wilson's foreground galaxies were selected with two color photometry while the background galaxies were selected by luminosity [30]. Therefore, the two results agree despite two different measurement methods.

The rotation velocity calculated for the blue galaxies at $z = 0.5$ is 216^{+49}_{-64} km/s for an Einstein-deSitter cosmology and 201^{+46}_{-59} km/s for a dark energy cosmology.

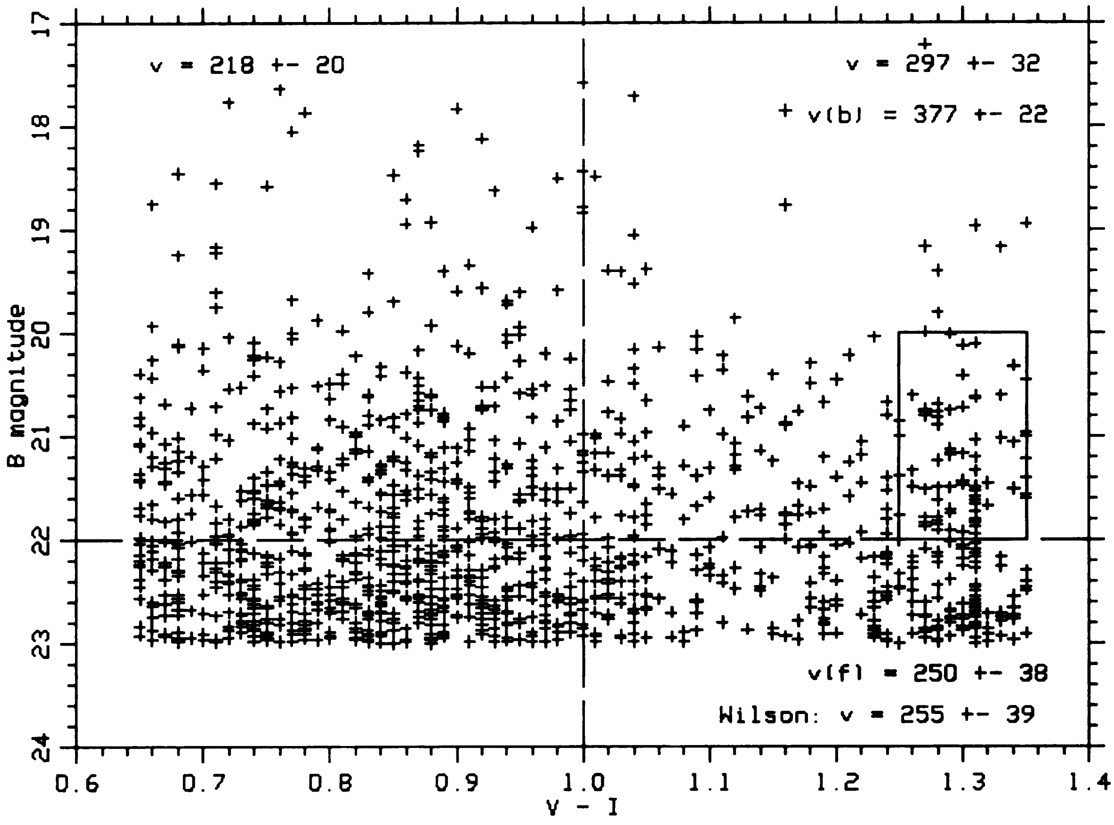

Figure 3.5: A color-magnitude diagram of the foreground galaxies selected by Wilson *et al.* [30] and the foreground galaxies selected by this work. The small box represents the galaxies selected by Wilson *et al.*. The vertical dashed line represents the separation between red and blue galaxies. The horizontal dashed line represents the separation between bright and faint galaxies.

These values are distinct from the rotation velocities for the red galaxies at $z = 0.5$. Again, Wilson *et al.* have no results for blue galaxies [30].

3.3 Alternate Depletion Sources

There are processes other than gravitational lensing depletion that could either reduce or increase the number density of background galaxies near foreground galaxies. These alternate sources of depletion are described and discussed in the following sections.

3.3.1 Blocking by Foreground Galaxies

A depletion in the number of background galaxies could be caused by large foreground galaxies biasing detection of background galaxies. The resulting depletion curve would show no depletion outside the radius of the foreground galaxy and a fairly sharp depletion inside the radius of the galaxy.

The measured depletion is not caused by foreground galaxies blocking background galaxies. Figure 2.8 shows the area of the galaxies. The brightest galaxies between $z = 0.1$ and $z = 0.3$ are at 18th magnitude. The maximum area of an 18th magnitude galaxy is 400 arcseconds. This area translates into a radius of $\frac{20}{\sqrt{\pi}}$ arseconds, or 20 kpc at $z = 0.2$. The data show measurable depletion out to 60 arcseconds, or 100 kpc at $z = 0.2$. This depletion range is much beyond the reach of even the largest foreground galaxies. Therefore, the measured depletion is not caused by foreground galaxies blocking background galaxies.

3.3.2 Blocking by Saturated Stars

Saturated stars could contaminate the baseline number density of background galaxies. Saturated stars completely wash out their immediate surrounding area so that no galaxies are found at all. This masking has the effect of reducing the number of background galaxies counted in the image and reducing the baseline number density. As a result, the angular correlation measured around foreground galaxies would be too high.

Saturated stars in this sample do not block enough background galaxies to contaminate their number density. First, as shown by Figure 2.9, saturated stars block a small area of the sky. Given the size and number of saturated stars, they cover 66,000 pixels out of 270 million, or 0.02 percent of the sky. Second, if there was a problem with saturated stars blocking background galaxies, then the baseline number of background galaxies measured in the sample would be artificially low. If the

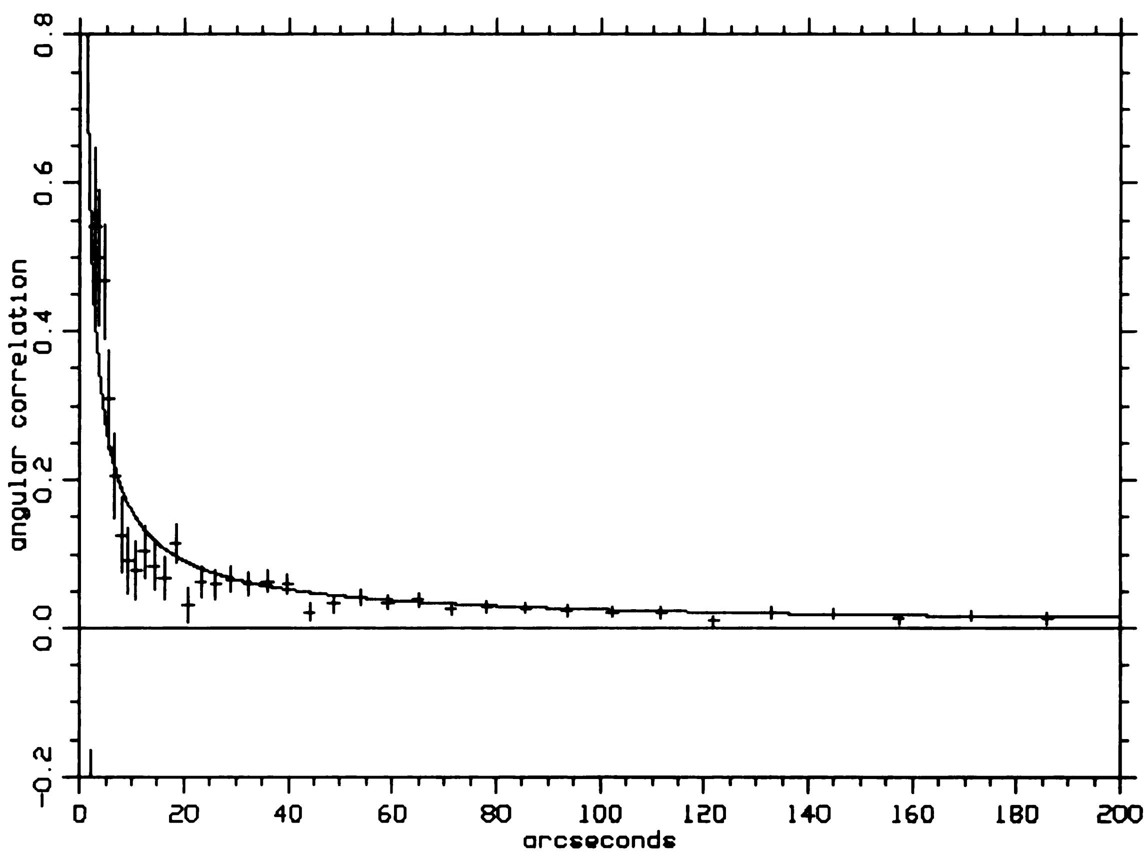

Figure 3.6: Autocorrelation of galaxies with $z > 0.6$. The fit is $\theta^{-0.8}$, the expected autocorrelation function of galaxies.

baseline number of background galaxies is low, then the angular correlation far from foreground galaxies would be positive because too many background galaxies would be counted. The data show that the angular correlation approaches zero at large distances as expected. Therefore, saturated stars are not adversely affecting the depletion measurements.

3.3.3 Cross-contamination

Contamination of the foreground or background samples can reduce the measured depletion. Figure 3.6 shows the autocorrelation of the galaxies at $z > 0.6$. Galaxies cluster together, so the autocorrelation of galaxies follows the form $\theta^{-0.8}$. The angular correlation between galaxy samples will rise if contamination between samples is large.

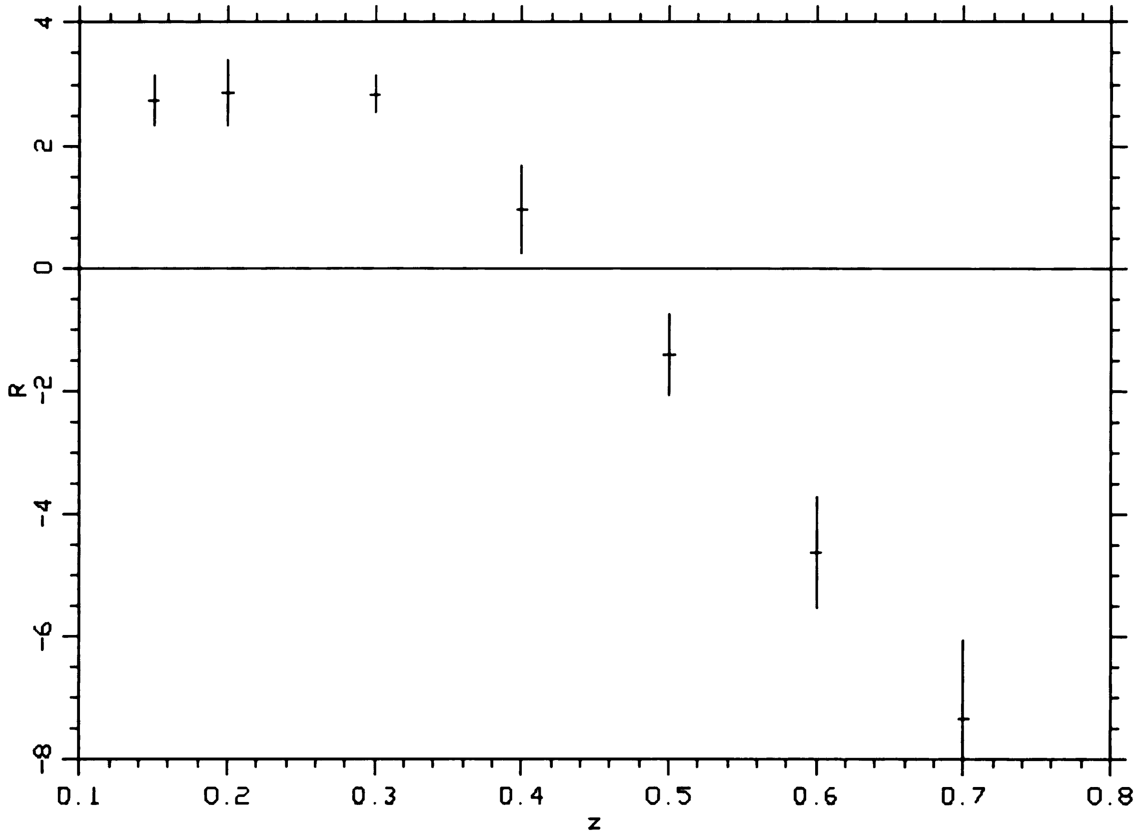

Figure 3.7: The best-fit r versus redshift. The r can be converted to Einstein radius if it is positive. Otherwise, it stands as a measure of correlation between the two samples. The width of each bin is 0.2.

There is no contamination between our background and foreground samples. Seven different groups of red foreground galaxies from $z = 0.15$ to $z = 0.7$ were correlated with a background sample at $z > 0.6$. The best-fit r is plotted against the median redshift of the foreground sample in Figure 3.7. For low redshifts, r is unchanging. As redshift increases past $z = 0.4$, the autocorrelation increases due to galaxies in one sample being related to galaxies in the other sample. Beyond a redshift of 0.5, some galaxies are placed in both foreground and background bins. The increase in autocorrelation results in smaller r, until the last few are unphysical negative numbers. Therefore, these depletion measurements are not contaminated by misplaced galaxies.

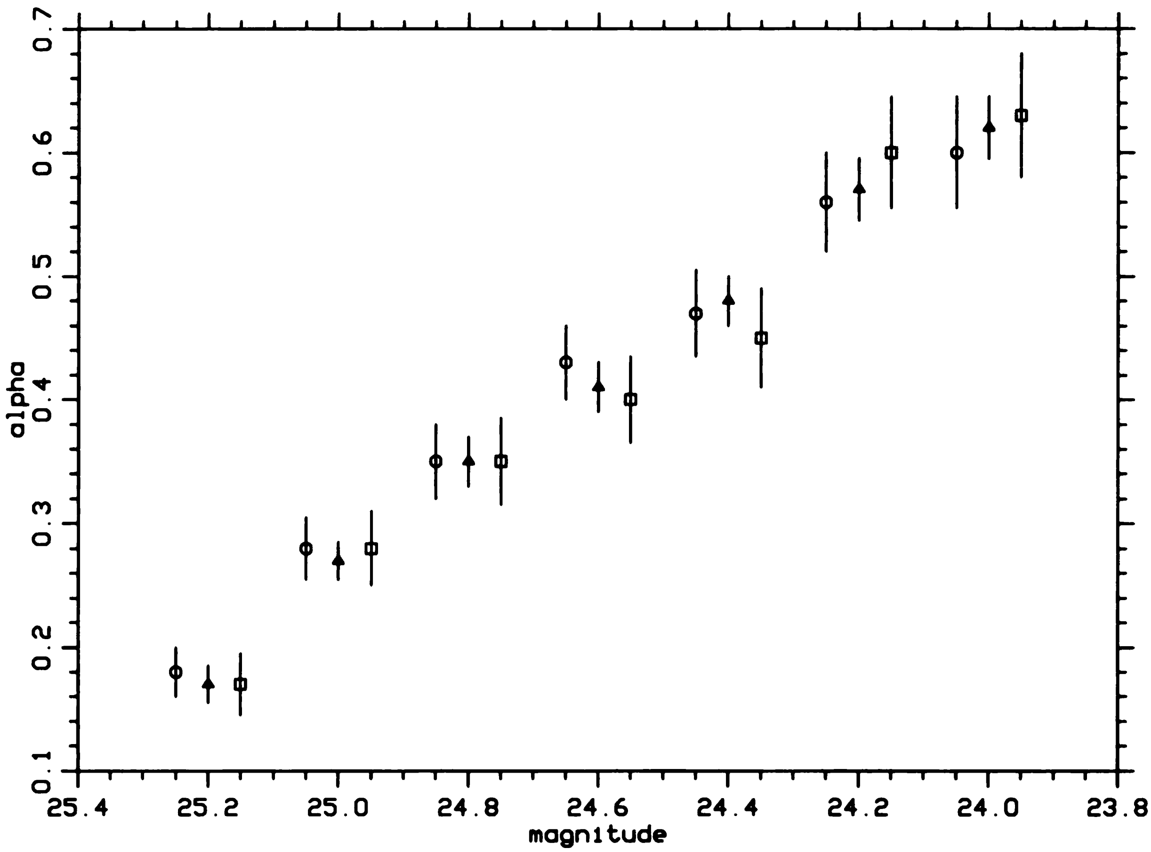

Figure 3.8: A plot of α vs. magnitude. The difference in magnitude used to calculate α is 0.2. The triangles represent all galaxies with $z > 0.6$, the boxes represent the red galaxies, while the circles represent blue galaxies.

3.4 The Effect of Varying α

This section checks the effect the value of the constant α has on the calculated Einstein radius. As a check on previous calculations, α was calculated for a number of magnitudes for galaxies with $z > 0.6$. Then, the background galaxies were split into blue and red bins and α was calculated for each color.

The rate of change of the number of background galaxies with magnitude is not constant. Figure 3.8 is a plot of α vs. magnitude. The calculated value of α shows a clear magnitude dependence. This magnitude dependence also shows up in the luminosity function. Figure 3.9 is the luminosity function for the galaxies with $z > 0.6$. There is not an area where the rate of change in the number of galaxies levels

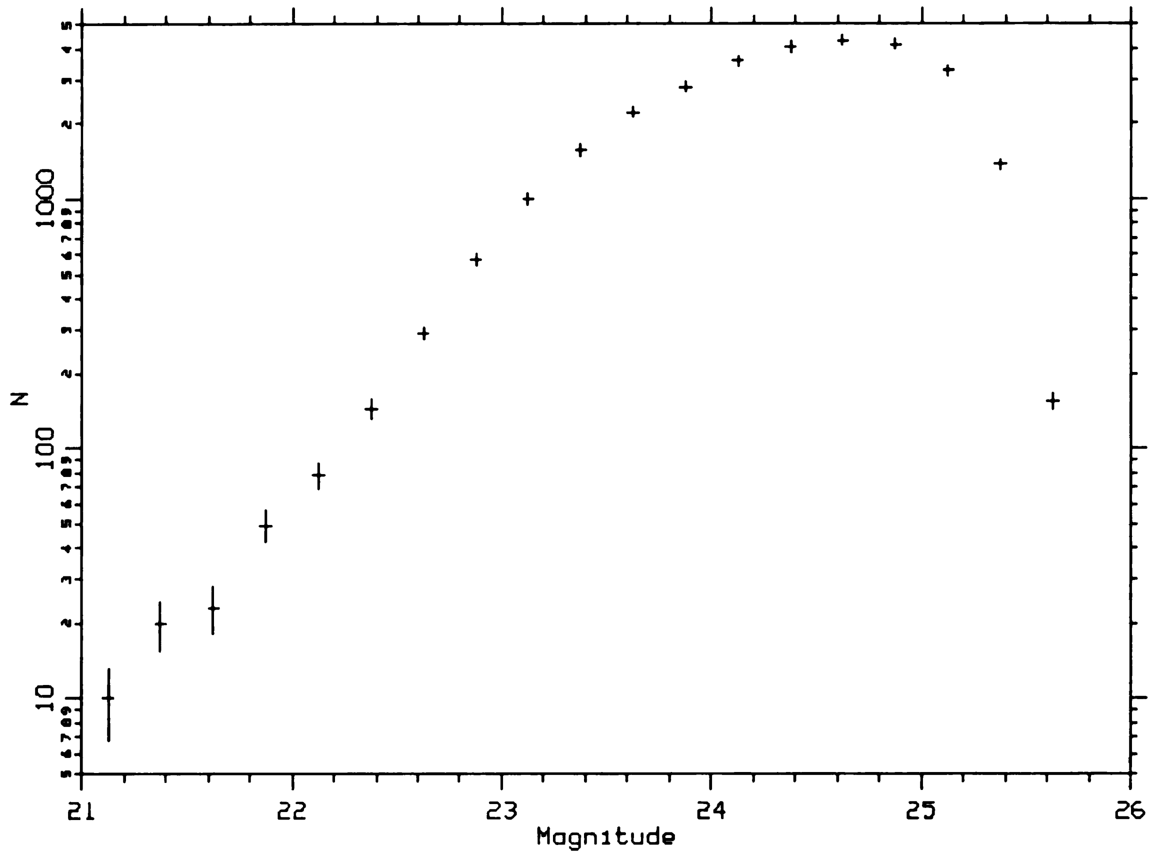

Figure 3.9: The luminosity function for galaxies with $z > 0.6$.

off, so this plot shows that there is some kind of slope in α. Furthermore the values of α are independent of color.

The magnitude dependence of α and the color independence disagrees with previous observations. The value of α is $-0.4 \times \alpha_L$, where α_L is from the Schecter fit to the luminosity function [24]. Schecter gave a constant value of $\alpha_L = -1.25$ [25], while observations from the 2dF survey suggest α_L ranges from -0.7 to -1.7, depending on galaxy type [11]. These values suggest that *alpha* can range from 0.28 to 0.68.

The value of α has a large effect on the best-fit Einstein radius. The Einstein radii for the near red and blue foreground galaxies is recalculated with a value of 0.17 for α instead of 0.27. The net result is to drop R_E by 20 percent with no change in the reduced χ^2 of the fit. The best fit Einstein radius for the near red sample drops to 1.7 ± 0.4, while the best fit for the near blue sample drops to 0.9 ± 0.2. These Einstein radii drop the rotation velocities to 240^{+26}_{-31} for the red sample and 176^{+15}_{-16} for the blue sample with a lambda-dominated cosmology. However, there is no clear reason to adopt this value of α instead of the value measured at the background cutoff, so the value measured at $B\mathrm{w} = 25$ will still be used.

3.5 Galaxy Mass

3.5.1 Red vs. Blue

The measured mass of red galaxies is greater than the measured mass of blue galaxies. The red galaxies have an average rotation velocity of 308 ± 30 km/s with a flat dark energy cosmology, while the blue galaxies have an average rotation velocity of 210 ± 35 km/s assuming the same cosmology. Both values are higher than the 225^{+12}_{-20} km/s for red elliptical galaxies and 144^{+8}_{-13} km/s for blue galaxies predicted by Fukugita and Turner [13]. However, if a reduced value of α is assumed as in the previous section, the two results for the rotation velocities are much closer. Fukugita and Turner predicted the rotation velocity of their galaxies by utilizing the luminosity function of Efstathiou, Ellis, & Peterson [7] and the Tully-Fisher relation [27].

The rotation velocity of the red galaxies is comparable with 255^{+36}_{-42} km/s reported by Wilson *et al.* [30] assuming a dark energy cosmology. However, the uncertainties on both sets of measurements are so large that the rotation velocity reported by Wilson *et al.* is consistent with the rotation velocity of the blue galaxies. Again, Wilson's sample consisted of bright elliptical galaxies selected by V-I color.

The ratio of red/blue rotation velocity is 1.5 ± 0.4, comparable to the ratio of the red and blue galaxies reported by Fukugita and Turner of 1.6 [13]. Therefore, while the measured rotation velocities of galaxies appears a little high, the ratio of red and blue rotation velocity agrees with the ratio of the red and blue rotation velocities reported by Fukugita and Turner. Furthermore, if a smaller value of α is assumed, the two results agree.

Finally, the measured rotation velocities are not inconsistent with the rotation velocities from the Sloan Digital Sky Survey. Fischer *et al.* measured the shape distortion of background galaxies several hundred arcseconds away from foreground galaxies. They measured a rotation velocity of 240 ± 28 km/s for foreground galaxies. They did not separate foreground galaxies by color, so this velocity is an average of red and blue galaxies [10]. The average of the red and blue rotation velocities in this measurement is 273 ± 35 km/s for an Einstein-deSitter cosmology, and 259 ± 33 km/s for a flat dark energy cosmology. Both results are consistent with the SDSS result.

3.5.2 Near vs. Far

No matter what cosmology is assumed, the measured mass of red galaxies at $z = 0.2$ agrees with the measured mass of red galaxies at $z = 0.5$. This result coincides with the lack of mass evolution reported by Wilson *et al.* [30]. Lilly *et al.* reported no luminosity evolution in galaxies redder than Sbc out to a redshift of $z = 1$ [20]. Therefore, these results indicate that the mass-luminosity relation for red galaxies does not change out to $z = 0.5$.

The measured mass of blue galaxies at $z = 0.2$ is the same as the measured mass of blue galaxies at $z = 0.5$ for both assumed cosmologies. Lilly *et al.* report that galaxies bluer than Sbc get brighter at $z > 0.5$. At $z < 0.5$, there is no change in luminosity of blue galaxies [20]. These results indicate that the mass-luminosity relation for blue galaxies also does not change out to $z = 0.5$.

3.5.3 Bright vs. Faint

The sample of near red galaxies was separated into bright and faint samples. The bright sample consists of galaxies with $B\mathrm{w} < 22$ between $z = 0.1$ and $z = 0.3$. The

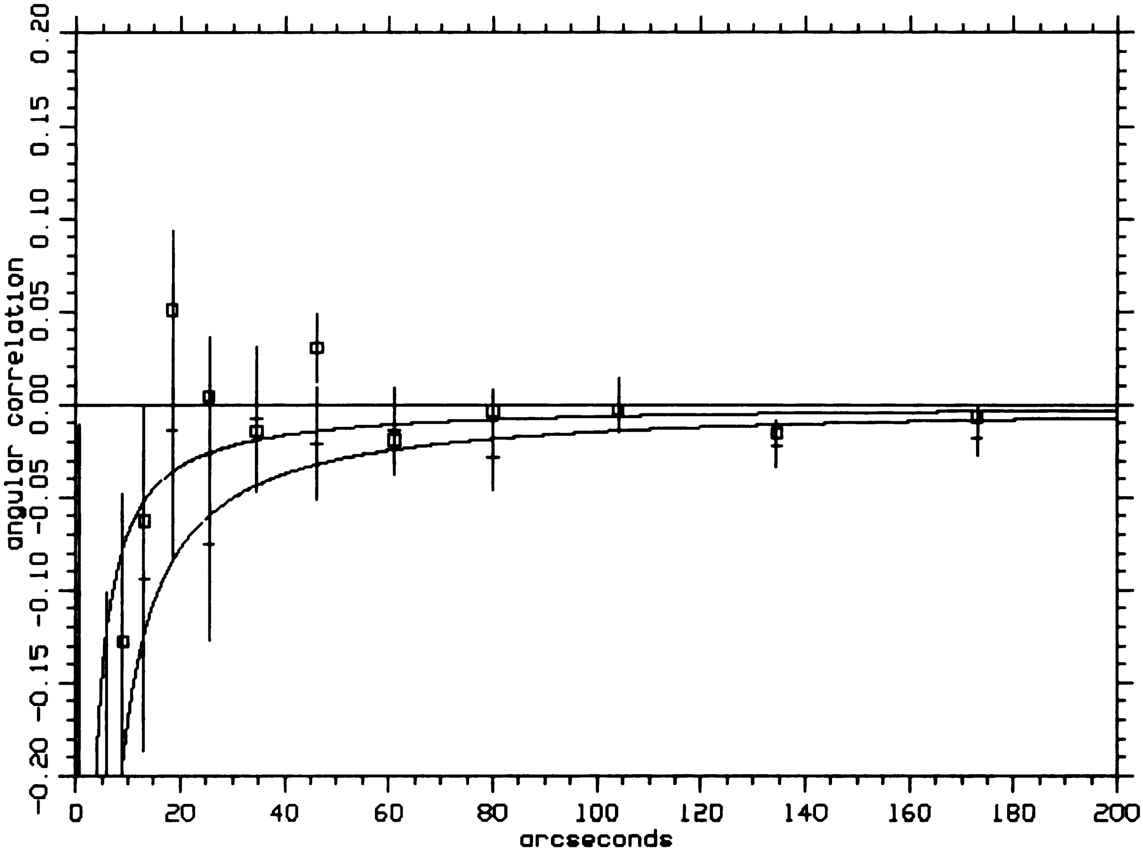

Figure 3.10: Bright (+) and faint (□) red galaxies at $z = 0.2$ are correlated with background galaxes beyond $z = 0.6$. The curves are the best fits to each population.

cutoff for the bright sample is 1 magnitude fainter than $m^* = 21$ for galaxies between $z = 0.1$ and $z = 0.3$. The faint sample consists of galaxies with $22 < B\mathrm{w} < 24$ between the same redshift limits. The cutoff for the faint galaxies is 3 magnitudes fainter than m^*.

The mass difference between the bright and faint samples follows the Tully-Fisher relation [27]. The Tully-Fisher relation states that $M = -10 \log v + C$, where C is a constant [13]. Velocity is proportional to $r^{0.5}$ according to Eq. 4.2. Therefore, $M = -5 \log r + D$, where D is a constant different from C. It follows from this equation that $M_{\mathrm{bright}} - M_{\mathrm{faint}} = -5(\log(r_{\mathrm{bright}}) - \log(r_{\mathrm{faint}}))$. The median magnitude is 21.2 for the bright group and 23.1 for the faint group. The best-fit Einstein radius is 4.1 ± 0.5 for the bright group and 1.8 ± 0.6 for the faint group. The median magnitude difference between the two groups is 1.9. The magnitude difference estimated from the Einstein radius difference is 1.7 ± 0.4. Therefore, the galaxy mass increases with luminosity and follows the Tully-Fisher relation.

3.6 Summary

The measurement of galaxy-galaxy lensing depletion yields many results. Red galaxies, with an average rotation velocity of 308 ± 30 km/s, are more massive than blue galaxies, with an average rotation velocity of 210 ± 35 km/s. Neither red nor blue galaxies exhibit mass evolution out to $z = 0.5$. Furthermore, the mass-luminosity relation appears to be constant out to $z = 0.5$. The rotation velocities of red galaxies at $z = 0.2$ follow the Tully-Fisher relation. The 258 ± 35 km/s average rotation velocity is consistent with the 240 ± 28 km/s average rotation velocity found by Fischer *et al.* [10]. The depletion measurements are not affected by saturated stars, contamination between foreground and background samples, or foreground galaxy size.

These rotation velocities may not be used to calculate the mass of the entire foreground galaxy. Instead, they may be used to constrain the mass within the area for which a depletion signal is present. The resolution of this measurement is too poor to differentiate between the small depletion signal present at 100+ arcseconds and no depletion signal. A larger sample of foreground and background galaxies will be needed to reduce the statistical errors.

Chapter 4

Conclusions and Future Work

A catalog of objects has been obtained from the NOAO Deep Wide Field. Three color photometry (Bw, R, and I) is available for the objects. Galaxies and stars have been successfully separated with few misclassifications for objects with a Bw magnitude brighter than 23.5. There are 29,163 objects classified as stars in the DWF. There are 57,685 objects classified as galaxies in the DWF. Photometric redshifts to $z = 1$ have been estimated for the galaxies.

Gravitational lensing depletion has been used to measure the rotation velocity of foreground galaxies in the Deep Wide Field. Red foreground galaxies have a mean rotation velocity of 313 ± 30 km/s, while blue foreground galaxies have a mean rotation velocity of 227 ± 40 km/s. The ratio of the rotation velocities of the red and blue galaxies is consistent with the ratio of the predicted rotation velocities of Fukugita and Turner [13], although the actual measured values of the rotation velocity are in both cases higher than the predicted values. There appears to be no change in rotation velocity for either set of galaxies out to a redshift of $z = 0.5$. The unchanging rotation velocity is consistent with the unchanging rotation velocities of bright elliptical galaxies found by Wilson *et al.* [30]. Finally, the rotation velocity of red galaxies with Bw < 22 is greater than the rotation velocity of the red galaxies with Bw > 22. The ratio of the rotation velocities of the bright and faint red galaxies matches the expected value from the Tully-Fisher relation.

There are a number of vital conclusions that can be drawn from this work. First, there is now a direct measurement of the rotation velocities of distant red and blue galaxies. The results of this measurement indicate that galaxies have not accrued mass since $z = 0.5$. The results also indicate that the relative masses of red and blue galaxies have remained unchanged over the same time period. Second, the rotation velocities of faint galaxies may be measured. Previous lensing measurements were limited to bright foreground galaxies. Third, because the mass of neither red nor blue galaxies appears to change to $z = 0.5$, and because Lilly*et al.* measured no luminosity evolution in either red or blue galaxies out to $z = 0.5$ [20], it appears that the mass-luminosity relation for galaxies holds out to $z = 0.5$.

Further work on the Deep Wide Field should reduce the uncertainties present in these results. Jannuzi and Dey are currently collecting spectroscopic redshifts in the DWF [16]. Spectroscopic redshifts may be used to directly check the accuracy of the photometric redshifts. Jannuzi and Dey are also working on infrared photometry of the DWF in the J (1-1.4 μm), H (1.4-1.6 μm), and K (2.0-2.4 μm) bands [15]. Infrared photometry will increase the number of available colors, improving the redshift fit. IR photometry will also allow the 4000 Å break to be measured for galaxies with a redshift greater than $z = 1$. The two effects may allow for lensing measurements for foreground galaxies at $z > 0.5$. This improved distance will check if blue galaxies evolve at $z > 0.5$ as expected.

Finally, Jannuzi and Dey will eventually release data for 54 fields [15]. Twenty-seven of those fields will be in the southern part of the sky instead of the northern sky. The increased number of fields and the varying location will reduce the statistical errors in the gravitational lensing measurements. The varying location will also reduce errors due to clustering that may have cropped up in this measurement.

Appendix A

Photometry and Photometric Redshift Techniques

A.1 Photometric Redshift Method

A.1.1 Background

The photometric redshift technique is an alternative to measuring redshifts spectroscopically. There are two main advantages to obtaining photometric redshifts. First, redshifts for large numbers of galaxies may be obtained from a few observations. Loh and Spillar noted in 1986 that redshifts for 200 galaxies could be obtained on the Wyoming 2.3m telescope in three hours [21]. The rate at which redshifts may be obtained is even greater with modern instrumentation and larger telescopes. Second, photometry has a fainter flux limit than spectroscopy. Therefore, redshifts may be obtained for fainter galaxies with the photometric method than with the spectroscopic method.

The most distinctive feature of a galaxy spectral energy distribution (SED) is the 4000 Å break. This break is due to metal lines and Balmer absorption in the galaxy, and appears as a sharp increase in galaxy luminosity as wavelength increases

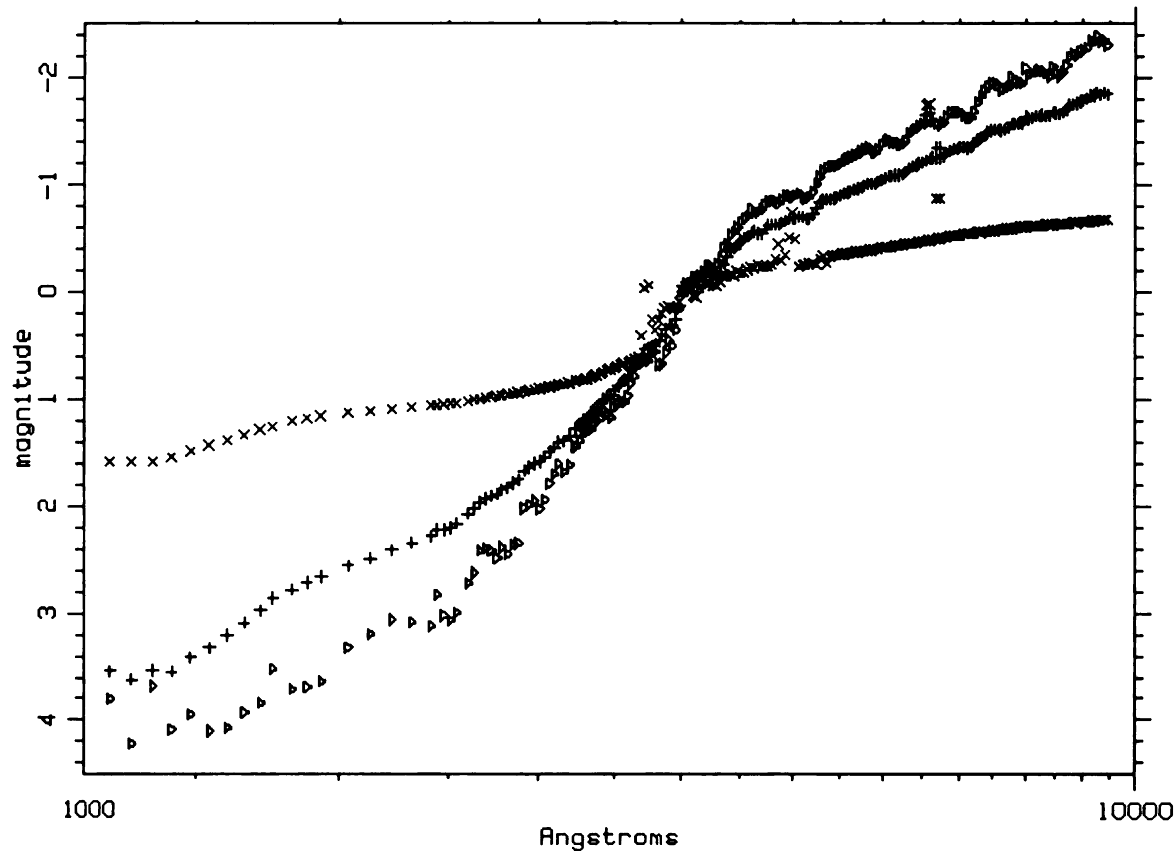

Figure A.1: Spectral energy distribution of an S0 galaxy (△), an Sbc galaxy (+), and an Im galaxy (X).

past 4000 Å [5]. Around 4500 Å the increase in luminosity levels off a little. The break appears to be present in all galaxies, so the position of the break in a galaxy's observed SED may be used as an indicator of redshift.

The goal of this Appendix is to check the photometric redshift and photometry techniques using a published data set. The photometric redshift technique is discussed first, followed by a discussion of photometry. Both techniques use the Hubble Deep Field as a practice data set.

A.1.2 Technique

This implemenation of the photometric redshift technique uses observed galactic spectra to create template SEDs. The effects of evolution are still uncertain, so

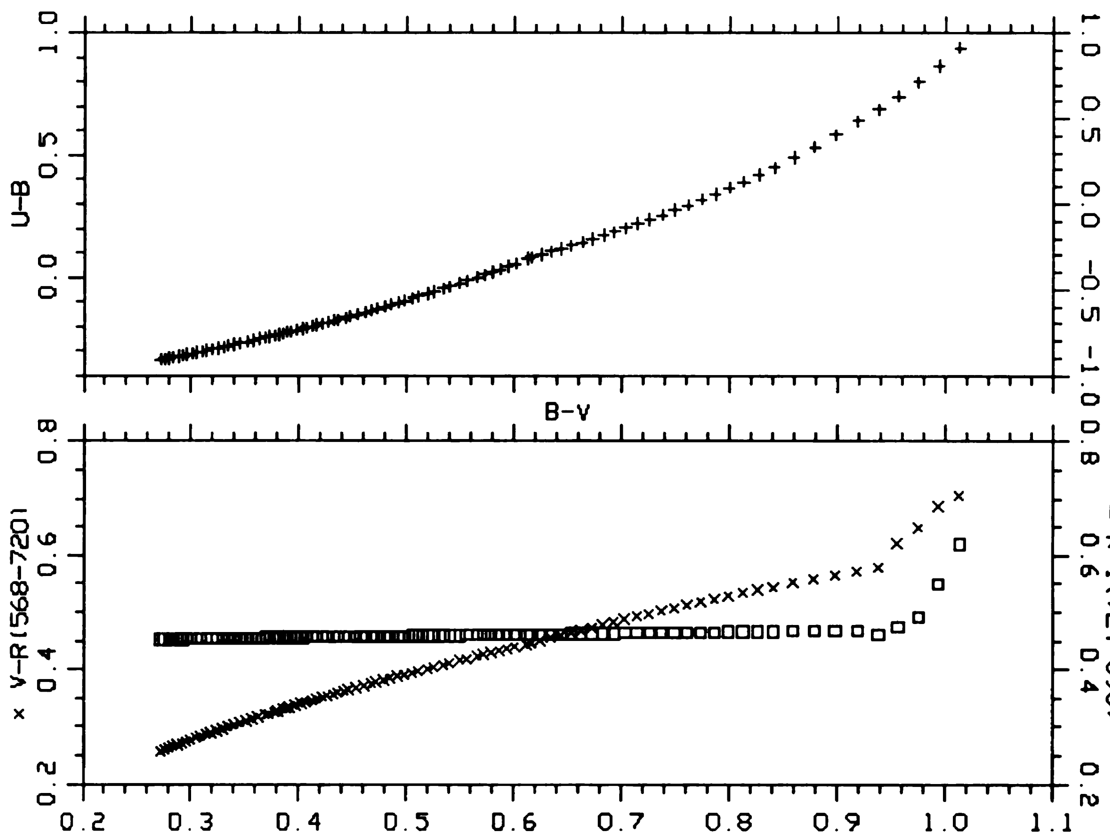

Figure A.2: A color-color plot of the template spectra. U-B (+, upper-left scale), V-R (×, lower left scale), and R-I (□, lower right scale) are plotted against B-V (both horizontal axes).

theoretical model spectra are not used in this implementation. The template spectra were observed by Kennicutt in 1992 [17]. The three template spectra are S0, Sbc, and Irregular (Im), and are plotted in Figure A.1.

The template SEDs are blended to recreate the fine graduations between real galaxy types. The flux of each galaxy template is normalized so that unit flux is at 4000 Å. Then, a composite galaxy is created with varying percentages of neighboring types. There are ninety total templates spanning the gaps between S0, Sbc, and Im. Figure A.2 plots the colors of the template spectra. The S0 has $B - V = 0.95$, the Sbc has $B - V = 0.71$, and the Im has $B - V = 0.30$.

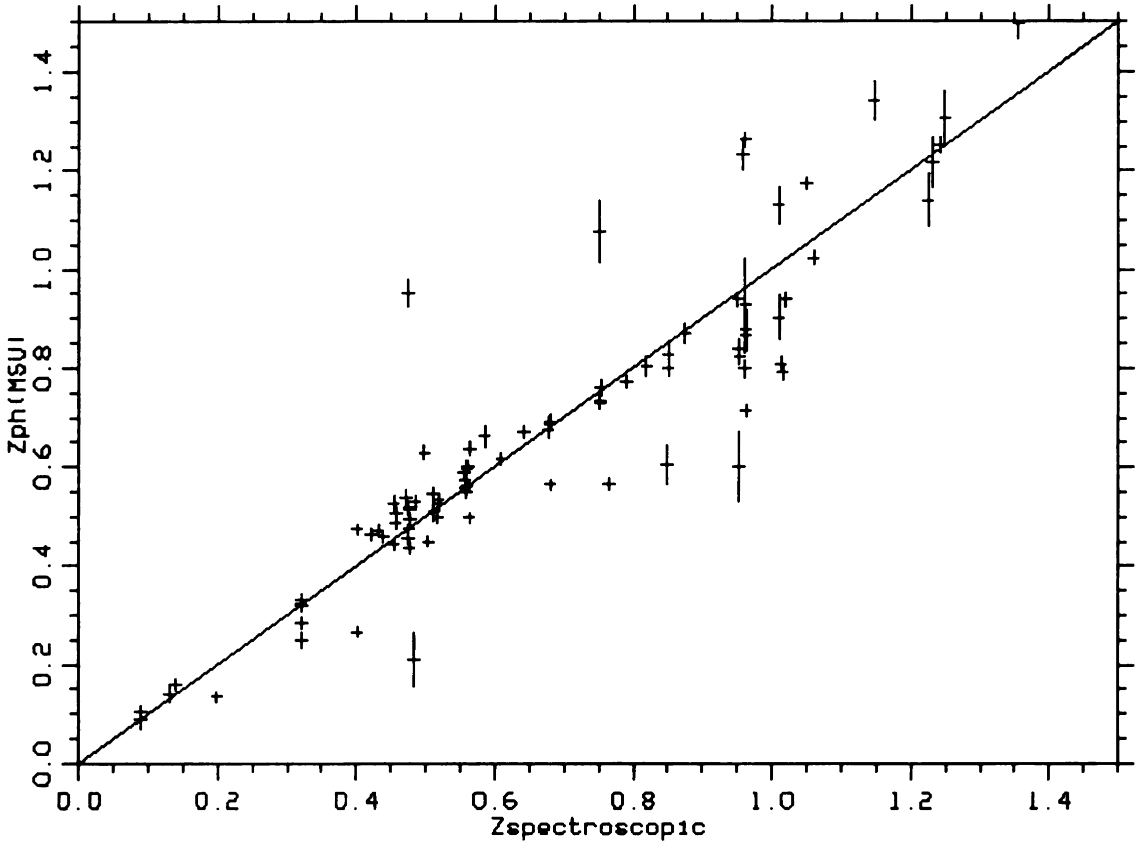

Figure A.3: Photometric redshifts produced by this method plotted against spectroscopic redshift.

Next, the template SEDs are redshifted by discrete amounts to recreate the expected observed redshifts. The fiducials ranged in redshift from 0 to 1.5 because the 4000 Å break is redshifted out of the visible filters around a redshift of 1 and there is a large gap in the available spectroscopic redshifts for the Hubble Deep Field after 1.5. A redshift spacing of 0.005 within these limits is the smallest spacing for which the χ^2 continues to decrease.

Finally, the fluxes of the redshifted SEDs are calculated for the filters used in the observation. The transmission percentage of a filter at a given wavelength is multiplied by the flux. This multiplication ensures the model flux matches the observed flux.

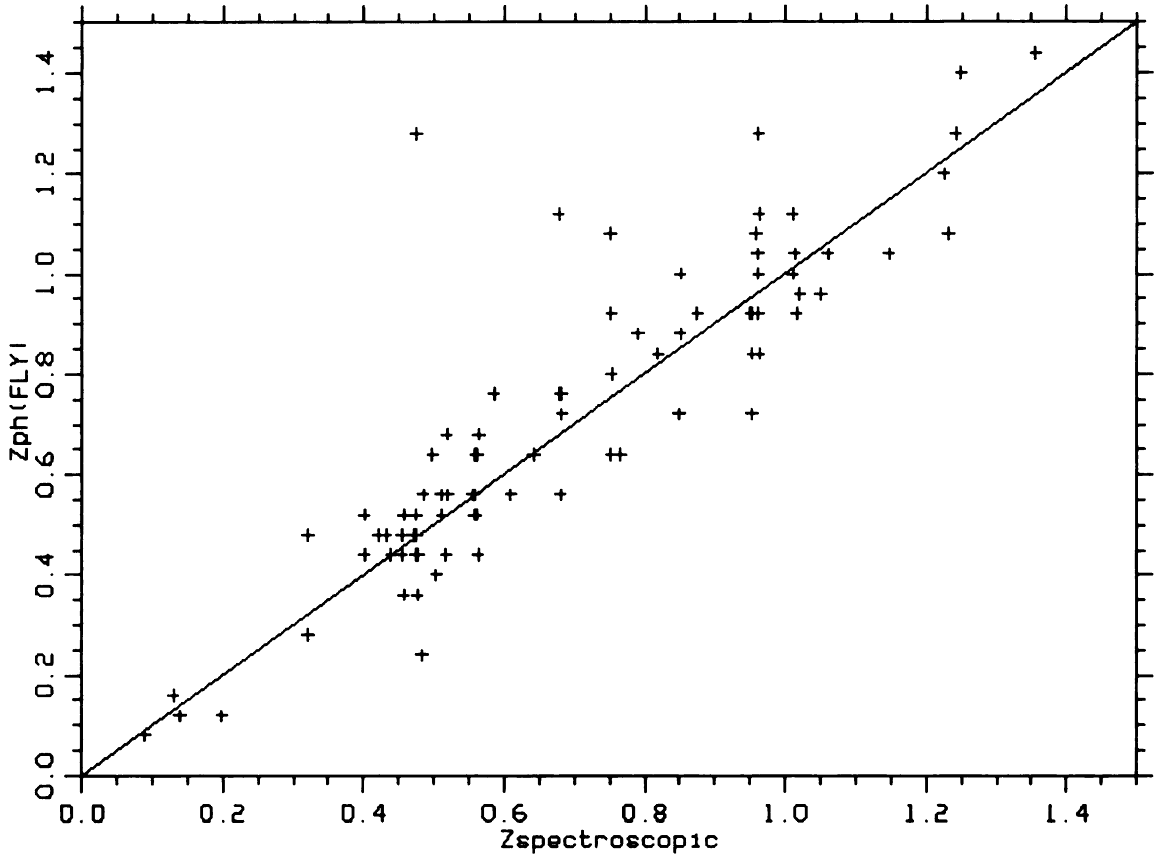

Figure A.4: Photometric redshifts produced by FLY plotted against spectroscopic redshift. A number of these spectroscopic redshifts were undetermined when the most recent FLY data were published.

A.1.3 The Hubble Deep Field

The Hubble Deep Field (hereafter referred to as HDF) images were taken in December 1995, and version 2 of the reduction was released to the public in February 1996 [29]. These images were taken with the Wide Field Planetary Camera 2 (WFPC2) on the Hubble Space Telescope through filters centered about 300, 450, 606, and 814 nm. These filters are referred to as F300W, F450W, F606W, and F814W, respectively. F300W is 72 nm wide, F450W is 93 nm wide, F606W is 158 nm wide, and F814 is 176 nm wide [2].

Shortly after the release of the version 2 data products, Fernández-Soto, Lanzetta, and Yahil (hereafter referred to as FLY) released their first set of photometric redshifts

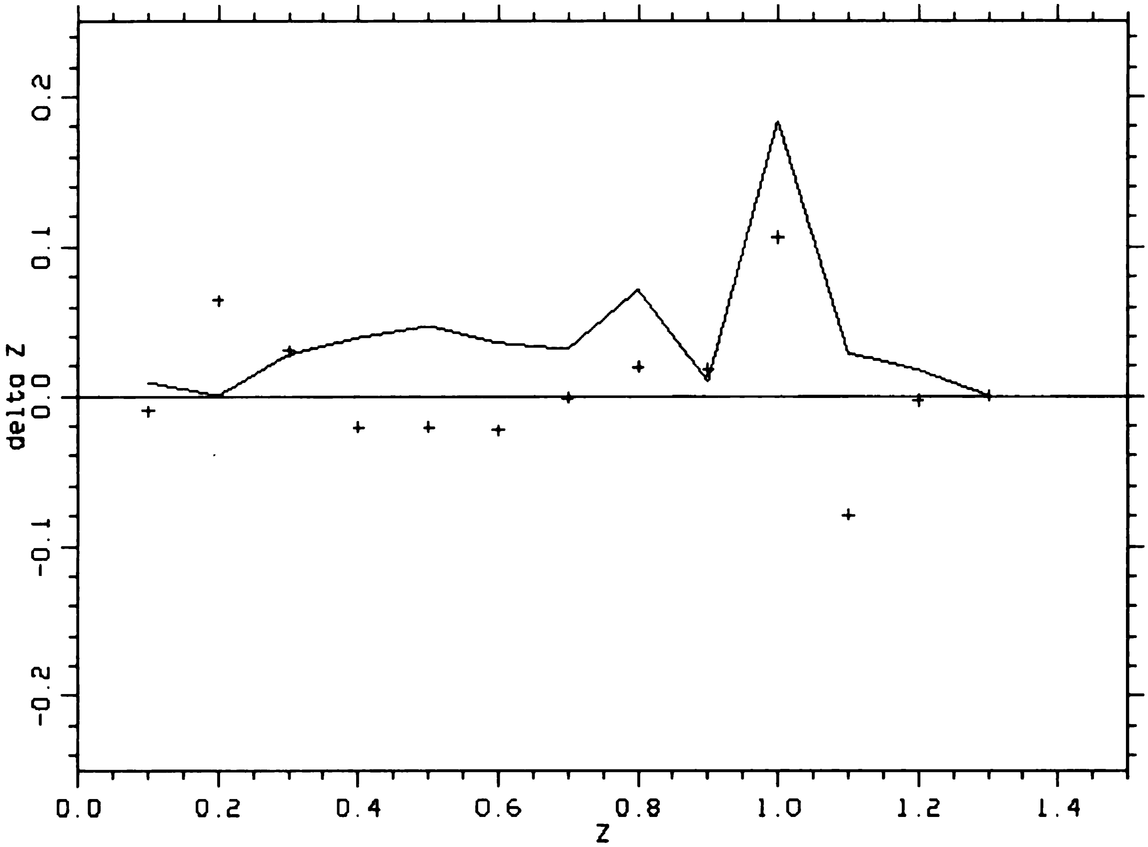

Figure A.5: Median error and dispersion of the photometric redshifts plotted against spectroscopic redshift. The median error is represented by (+), while the dispersion is represented by the line.

for the HDF [19]. In 1998, after obtaining J, H, and K band photometry of the HDF, FLY released improved photometric redshifts and photometry [9]. This latest release will form the basis of the redshift comparison.

A.1.4 Results

This section describes the results of applying this photometric redshift technique to the HDF. The analysis concerns galaxies for which spectroscopic redshifts are available. The redshifts are calculated with the STARGAZE software package.

The photometric redshifts computed with this technique agree with spectroscopic redshifts. Figure A.3 is a plot of photometric redshifts computed by this technique

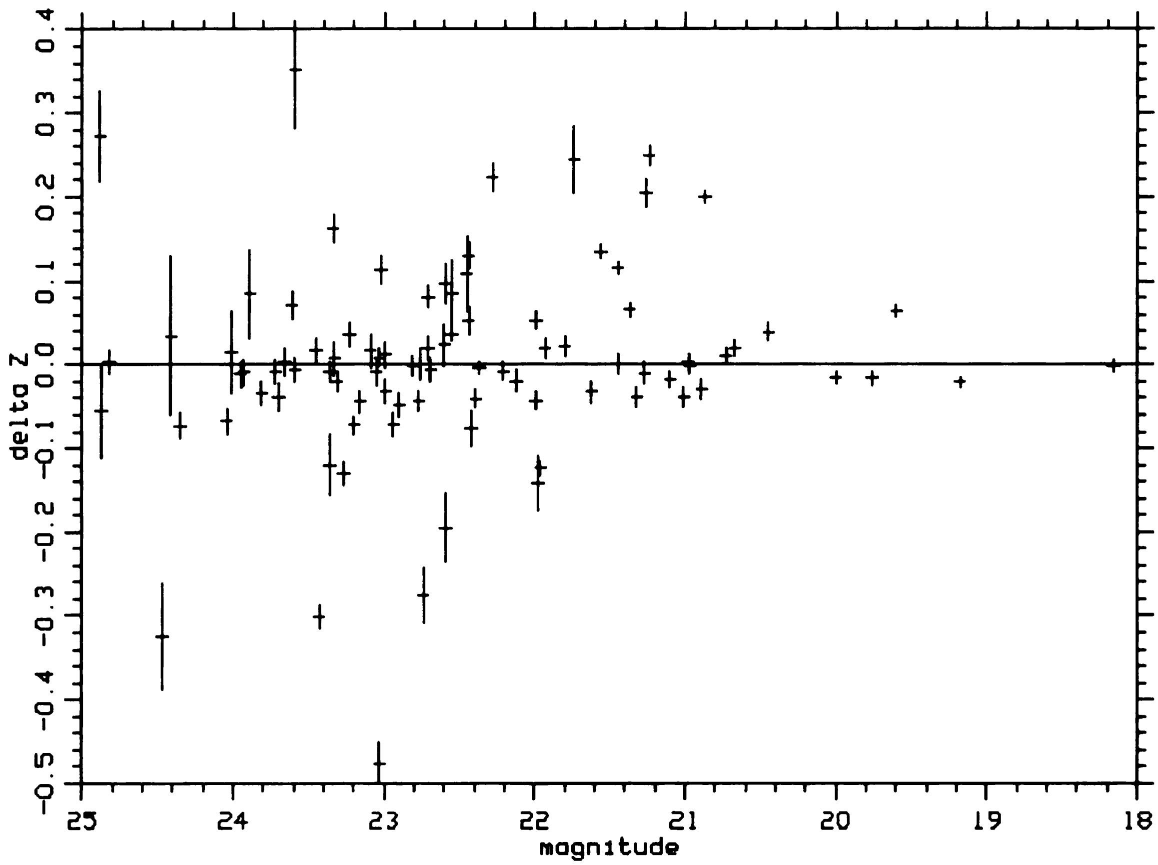

Figure A.6: The difference between spectroscopic and photometric redshifts plotted against magnitude.

versus spectroscopic redshift. Figure A.4 is a plot of photometric redshifts computed by FLY versus spectroscopic redshift. The median difference between photometric and spectroscopic redshift is 0.00 ± 0.08 for both groups of photometric redshifts. Therefore, on average, there is no bias between photometric and spectroscopic redshifts. Furthermore, the photometric redshifts are consistent with those calculated by FLY.

While there is no average bias between photometric and spectroscopic redshifts, there are some redshift regions that show a bias. Figure A.5 is a plot of the median of the difference between photometric and spectroscopic redshifts and the dispersion of the median redshift difference. At $z = 1$, the redshift is overestimated by a median value of 0.1. At $z = 1.2$, the redshift is underestimated by a median value of 0.08.

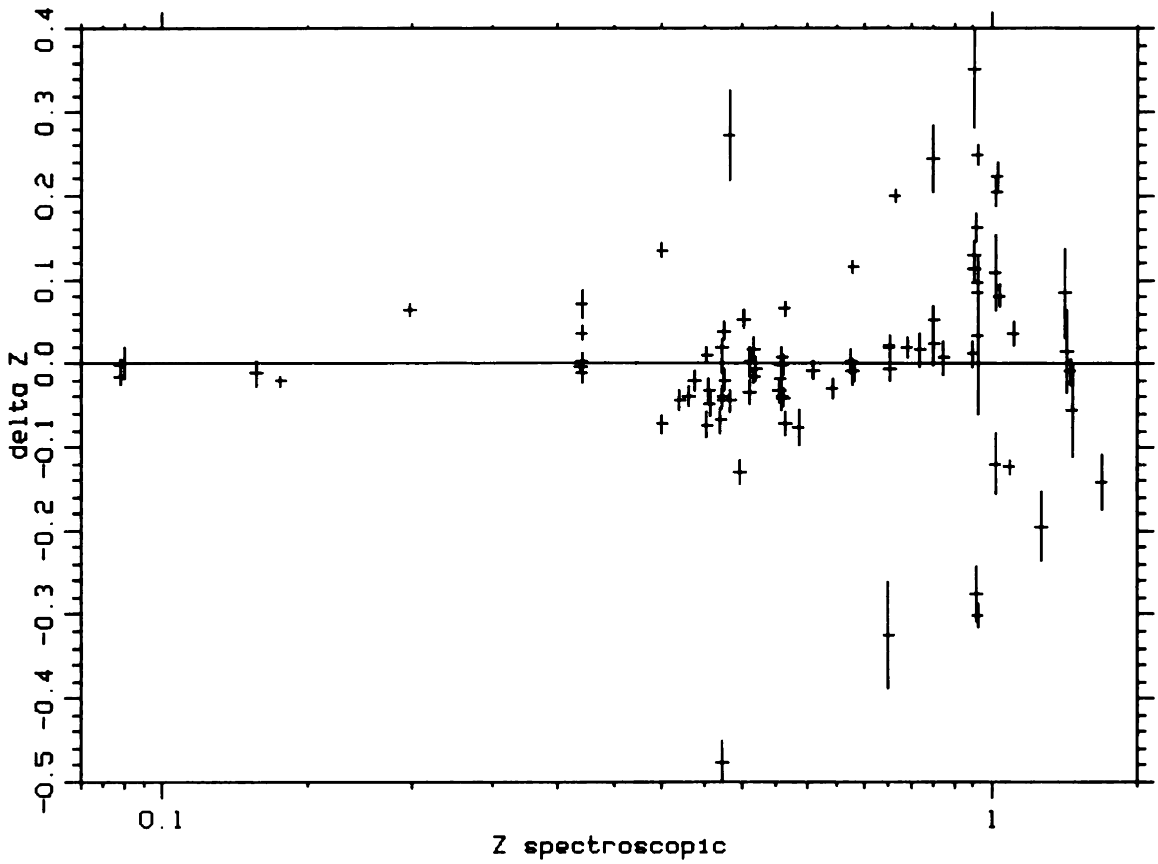

Figure A.7: The difference between spectroscopic and photometric redshifts plotted against spectroscopic redshift.

There is no bias at $z = 0.2$ because there is only one data point for that redshift. The median dispersion is greatest at a redshift of $z = 1$, indicating that the redshift fit is poorest for that redshift.

The spread in differences between the photometric redshifts and spectroscopic redshifts increases with magnitude. Figure A.6 is a plot of the difference between photometric and spectroscopic redshift versus magnitude. This spread is expected because photometric uncertainties are proportionial to $\frac{1}{\sqrt{\text{flux}}}$. Therefore, the spread in differences should increase as galaxies become fainter.

The spread in differences between the photometric redshifts and spectroscopic redshift increases with redshift. There are two causes for this spread. First, the higher redshift galaxies will be fainter due to increased distance. Second, the 4000 Å

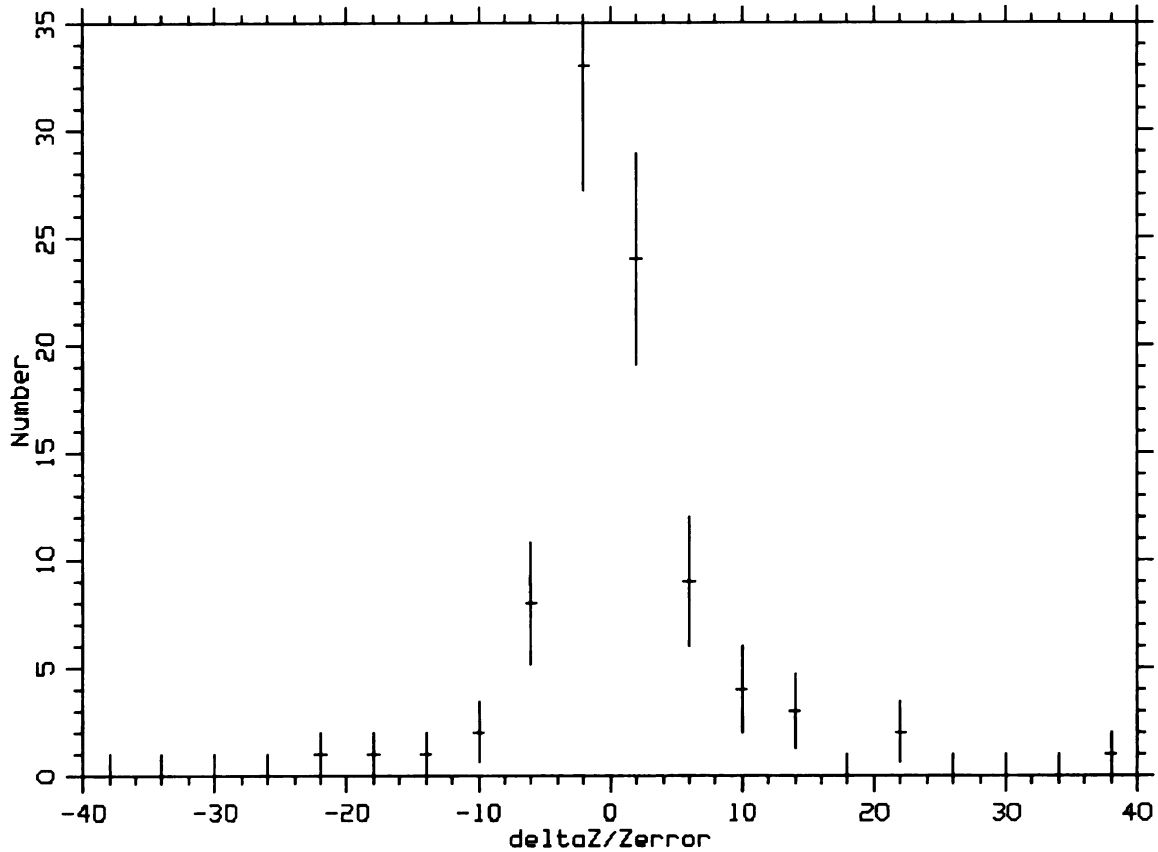

Figure A.8: A histogram of $\frac{z_{\text{spectroscopic}} - z_{\text{photometric}}}{\sigma z_{\text{photometric}}}$.

break is redshifted out of the F814 filter near $z = 1$. Therefore, the distinguishing feature used to determine photometric redshifts disappears from the photometry for galaxies farther than $z = 1$. Figure A.7 shows that the spread in differences becomes much larger at $z = 1$, confirming this hypothesis.

The calculated uncertainty in photometric redshifts is not representative of the difference between photometric and spectroscopic redshift. The calculated uncertainty is derived from the photometric errors. Figure A.8 is a histogram of the difference between spectroscopic and photometric redshift divided by the photometric redshift uncertainty. The histogram is centered about 0 ± 5. The FWHM of the histogram is 8. The expected FWHM is $2\sqrt{2 \ln 2} * \sigma$, or 2.4. Therefore, the average differences between spectroscopic and photometric redshift are 3.4 times larger than expected.

A.1.5 Conclusion

The photometric redshifts calculated for the Hubble Deep Field agree with spectroscopic redshifts as well as previously published photometric redshifts. The calculated uncertainties are smaller than expected by a factor of 3.4.

A.2 Photometry Method

A.2.1 Background

The goal of this section is to check my photometry method using a data set that has already been published and analyzed. The Hubble Deep Field (HDF) serves as this data set. A description of the HDF is given in the previous section. Shortly after the release of the version 2 data products, Fernández-Soto, Lanzetta, and Yahil (FLY) released their first set of photometric redshifts for the HDF [19]. In 1998, after obtaining J, H, and K band photometry of the HDF, FLY released improved photometric redshifts and photometry [9]. This latest release will form the basis of the photometric comparison.

FLY used the Source Extractor (SExtractor) software package to perform photometry on the HDF. SExtractor is a program designed to "detect, deblend, measure, and classify sources" in astronomical images [1]. SExtractor was chosen to perform photometry on the HDF for its speed in handling large amounts of data and for consistency with the methods of FLY.

A.2.2 Description of Photometry

The two available photometry methods are isophotal photometry and aperture photometry. Isophotal photometry finds a source and divides it up by contours of equal brightness, or isophotes. All the light within a certain isophote is counted as

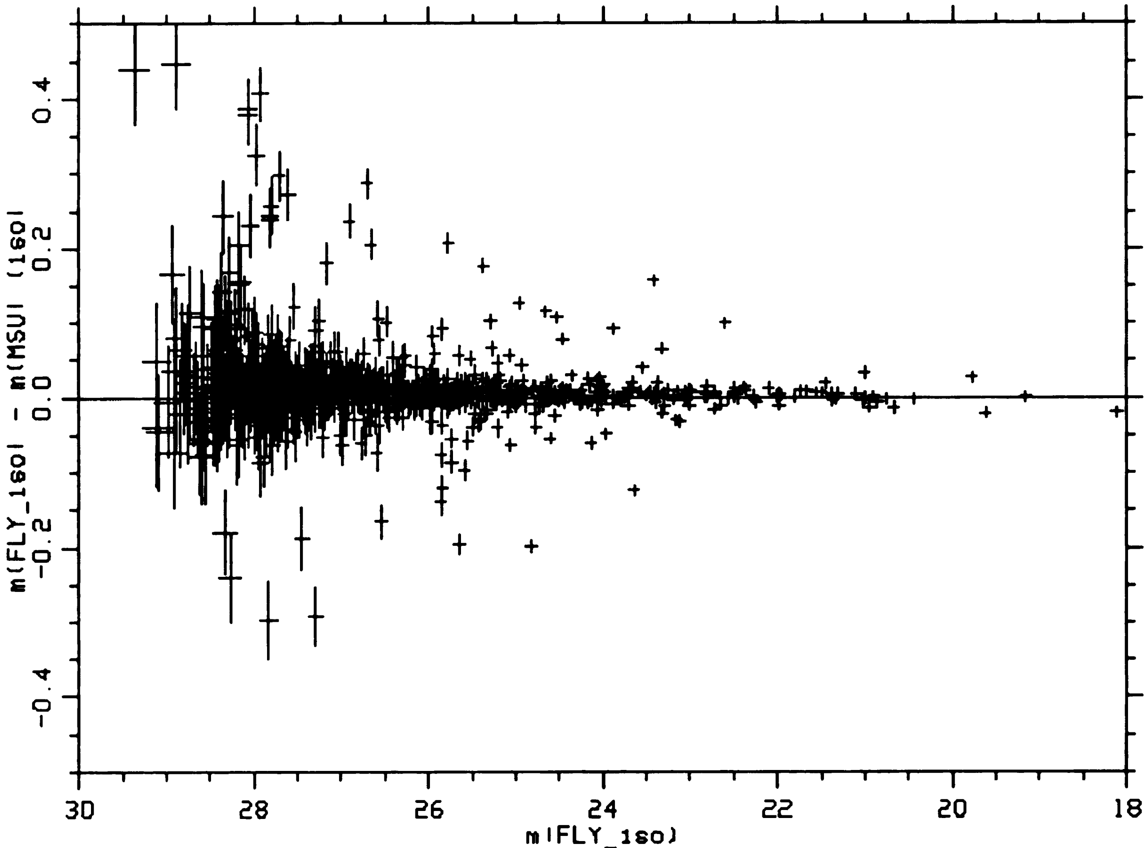

Figure A.9: The difference between FLY isophotal magnitudes and the isophotal magnitudes of this work plotted versus FLY isophotal magnitudes for 976 galaxies in the HDF.

the flux of the object. Aperture photometry finds a source and surrounds it with an aperture. All the light within that aperture is counted as the flux of the object.

SExtractor employs the following procedure to determine the background flux. First, it computes the local background histogram for a grid of size determined by the user. Then, the outliers are thrown out until the limits of the histogram are $\pm 3\sigma$ around the median. If σ of the new distribution is within 20 percent of the original σ, the field is considered uncrowded and the mean of the new histogram is the background. Otherwise, the background is estimated with:

$$background = 2.5 \cdot median - 1.5 \cdot mean \tag{A.1}$$

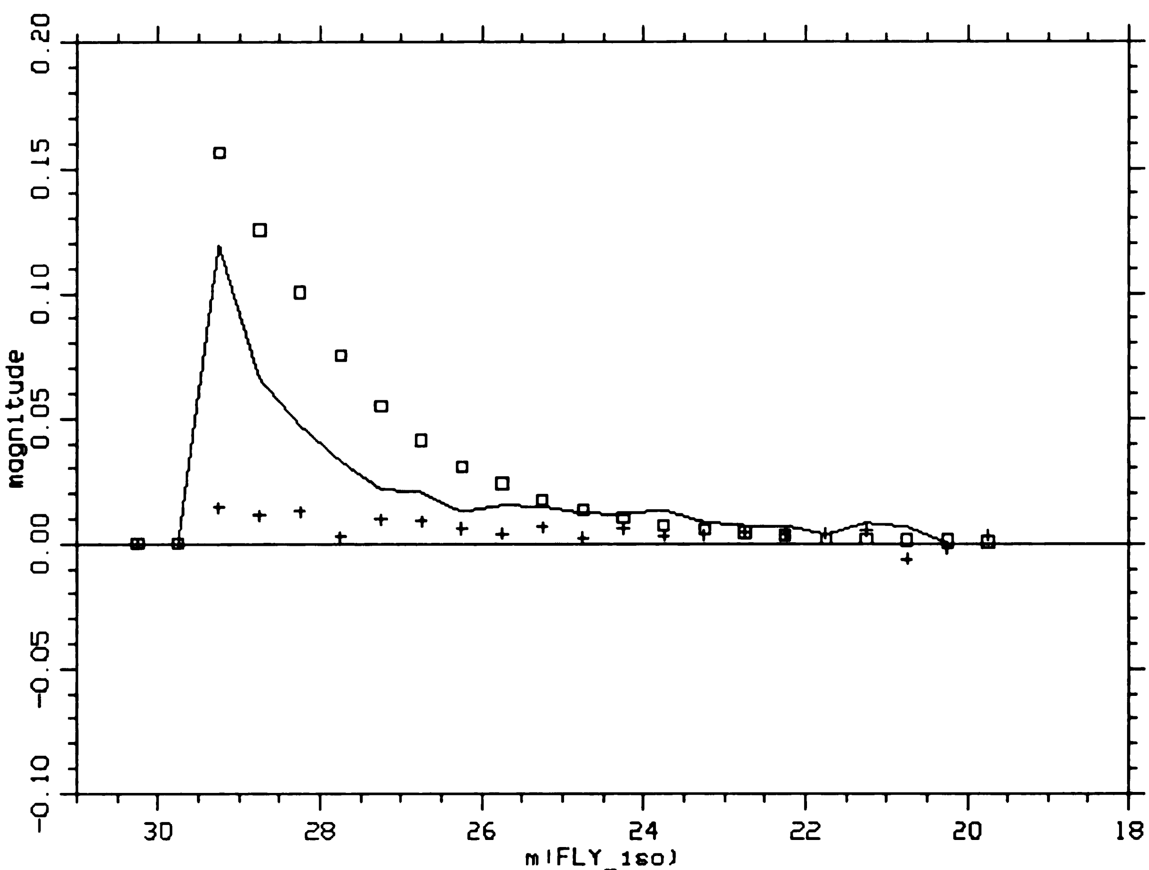

Figure A.10: The median difference between the two isophotal magnitudes (+), the dispersion of the difference (–), and the magnitude uncertainty (□) plotted versus FLY isophotal magnitudes for 976 galaxies in the HDF. The data are grouped into bins 0.5 magnitudes wide.

This background is subtracted from the measured flux [1].

A.2.3 Isophotal Photometry

FLY calculated their photometric redshifts using isophotal photometry. Therefore, isophotal photometry was performed on the HDF in an attempt to reproduce the FLY photometry.

The following steps were taken to reproduce the results of the FLY photometry. First, the parameters given in their first report were adopted. Namely, the images were smoothed by a gaussian filter of full-width half maximum (FWHM) 3 pixels. The

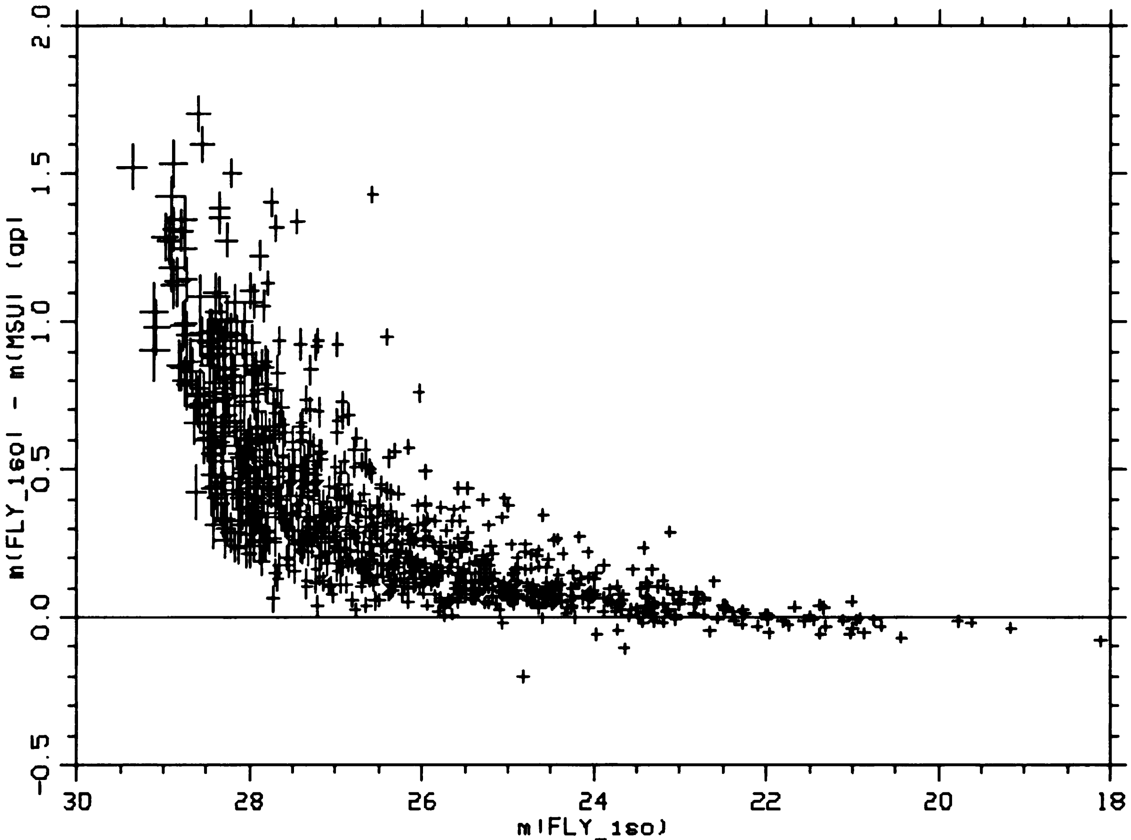

Figure A.11: The difference between FLY isophotal magnitudes and my aperture magnitudes plotted versus FLY isophotal magnitudes for 976 galaxies in the HDF.

detection threshold was set to at least ten pixels with a signal-to-noise ratio greater than 1.9 σ each. Furthermore, where two or more sources overlapped, the light from the overlapping pixels was excluded from both objects' photometry. Finally, the F814W image was used as a fiducial source map [19]. The area photometered in the other three colors was based on the source area found in F814W. FLY did not clearly specify a size for the background subsquares, so the background was measured in 72 $\times$ 72 pixel squares throughout the image. This size is large enough to surround the largest sources, but small enough to pick up some of the local variation in the background.

The next task was to match the resulting sources with the sources FLY found. This extraction found 2925 possible sources. FLY published results for 1067 sources.

They limited their sources to those above 26^{th} magnitude in the F814W band if they lie in a strip near the edge of the field, or above 28^{th} magnitude in the remainder of the field. The sources that had a center position within two pixels of sources found by FLY were flagged. This pruning left 976 sources common to both catalogs. These sources form the basis for the remaining analysis.

The isophotal magnitudes agree with those computed by FLY. Figure A.9 shows the difference between FLY isophotal magnitudes and the isophotal magnitudes of this work plotted against FLY isophotal magnitudes. There is little difference between the two results for bright galaxies. As the galaxies become fainter, the spread of differences increases. However, there does not appear to be a systematic shift toward brighter or fainter magnitudes between the two results.

There is no bias between the isophotal magnitudes and FLY isophotal magnitudes. Figure A.10 is a plot of the median of the difference between isophotal magnitudes and FLY magnitudes, the dispersion of the median of the difference, and the median magnitude uncertainty versus FLY magnitude. The median difference between magnitudes remains close to zero for all magnitudes and is never greater than the uncertainty in magnitude. Therefore, there is no bias present.

A.2.4 Aperture Photometry

Does aperture photometry result in different photometric redshifts? In theory, faint objects should appear brighter using aperture photometry. By definition, isophotal photometry omits light from a source that falls outside the isophote. Aperture photometry can count this light by utilizing a larger aperture, but the larger aperture will increase background noise. There will be a noticeable difference between measured magnitudes if the 1.9σ isophotal limit omits a sizable fraction of the flux of a source.

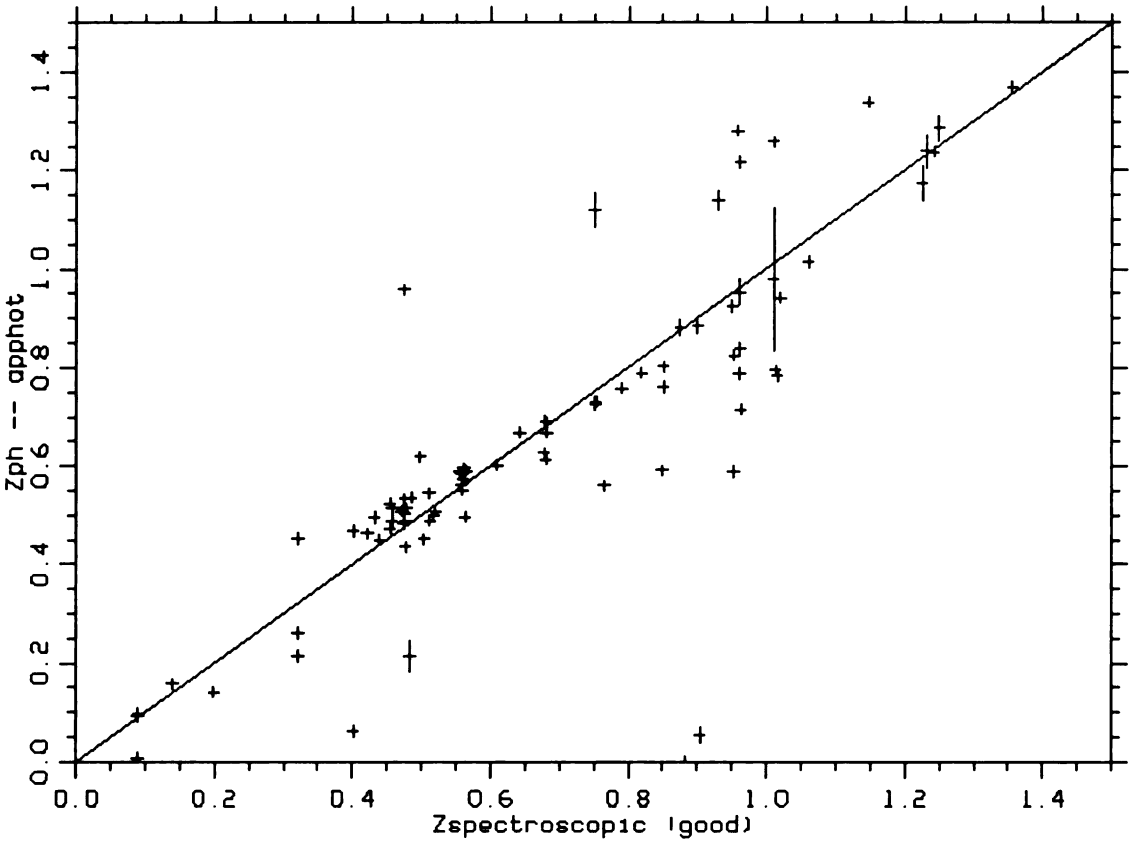

Figure A.12: Photometric redshifts calculated with aperture photometry plotted versus spectroscopic redshifts for 86 galaxies in the HDF.

The aperture surrounding each source is calculated in the following manner. First, an ellipse with ellipticity ϵ and position angle θ is defined to surround each source at its 1σ isophotal limit. Then, the radius of this ellipse is doubled. Within this aperture is calculated the "first moment:"

$$r_1 = \frac{\sum rI(r)}{\sum I(r)} \tag{A.2}$$

The aperture radius is kr_1. Most galaxies appear as ellipses in the sky, so elliptical apertures will maximize coverage and minimize background. Therefore, the axes are ϵkr_1 and kr_1/ϵ for an elliptical aperture. The scaling factor k determines the relative size of the aperture. The default $k = 2.5$ is used to maximize source coverage while

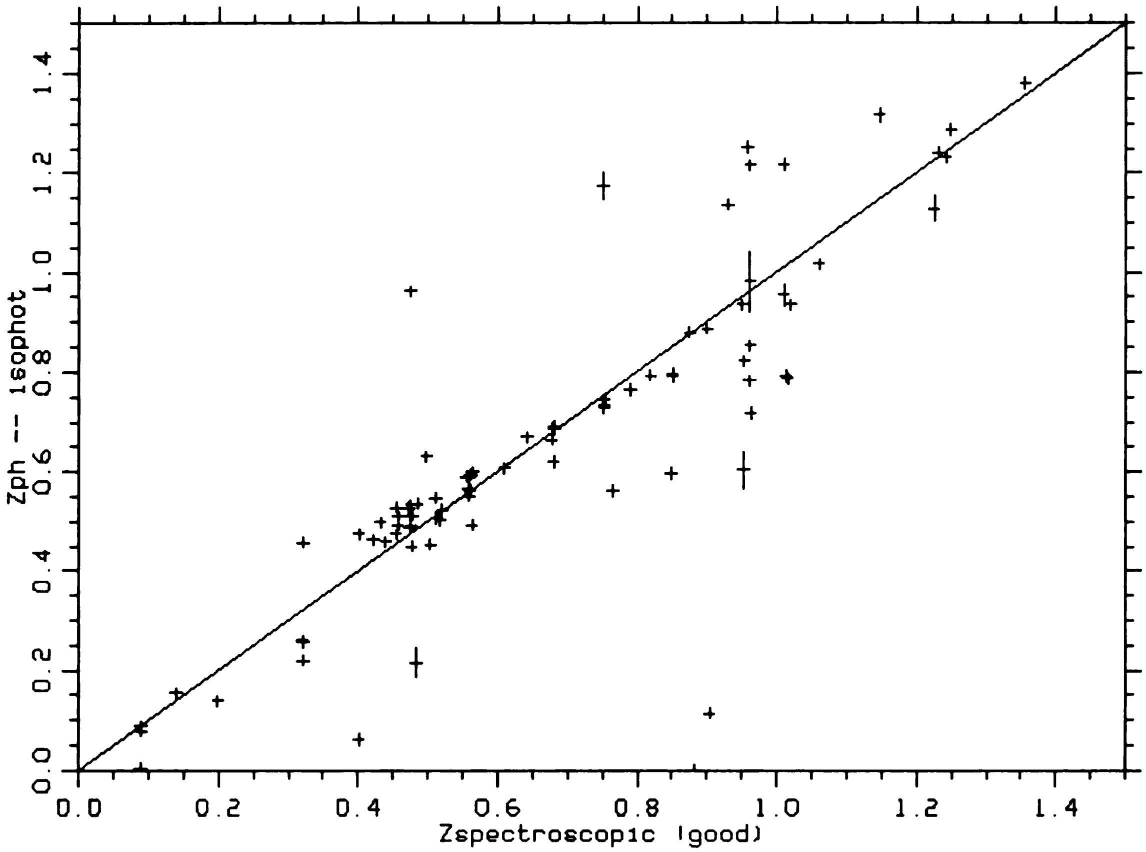

Figure A.13: Photometric redshifts calculated with isophotal photometry plotted versus spectroscopic redshift for 86 galaxies in the HDF.

minimizing the number of background counts included in the measurement of the source.

The results of FLY isophotal photometry and the aperture photometry of this work diverge for faint objects. Figure A.11 is a plot of the difference between FLY isophotal magnitudes and aperture magnitudes versus FLY magnitude. The median difference between FLY isophotal magnitudes and aperture magnitudes clearly increases for fainter sources. The aperture magnitudes are consistently brighter than the isophotal magnitudes for sources fainter than 25^{th} magnitude. Aperture magnitudes are expected to be brighter than isophotal magnitudes for faint sources, so this difference matches expectations.

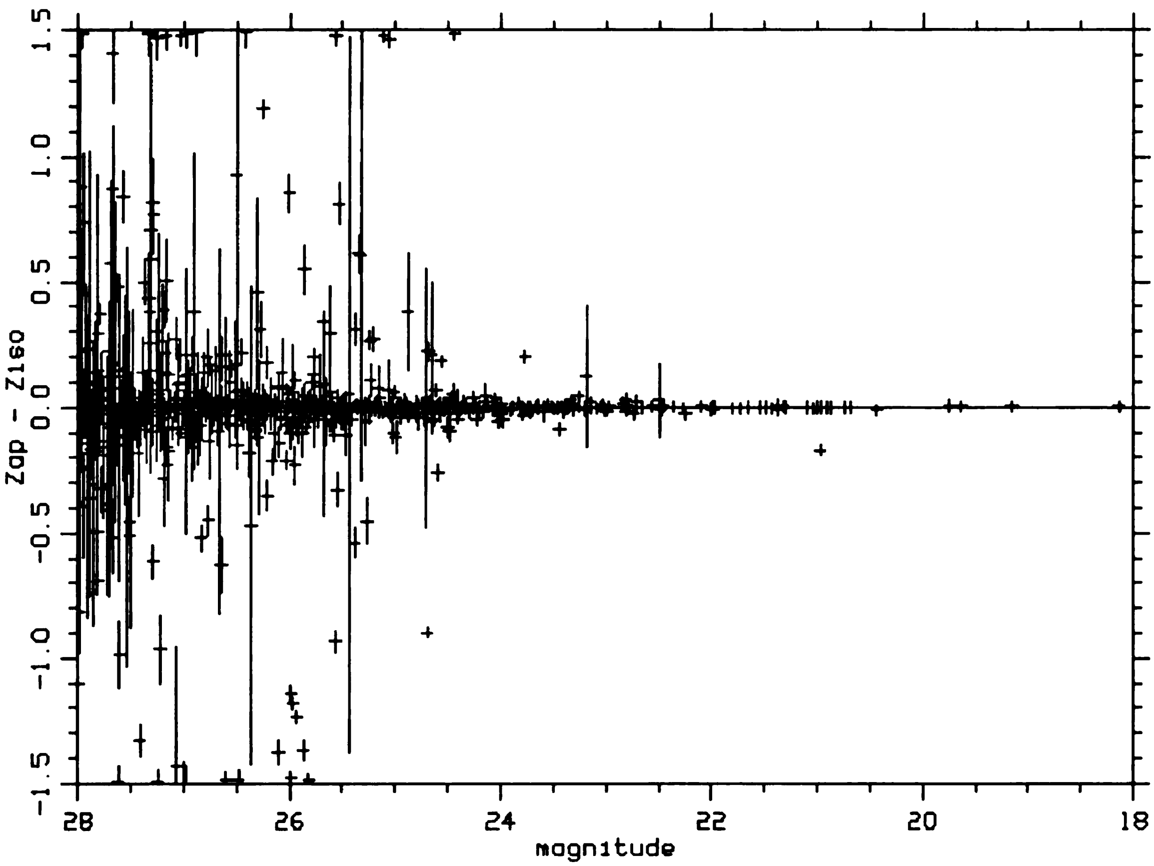

Figure A.14: $z_{\text{aperture}} - z_{\text{isophotal}}$ versus aperture magnitude for 976 galaxies in the HDF.

A.2.5 Photometry Comparison

The next step was to calculate photometric redshifts for these galaxies using the procedure described in Section 2.2. Photometric redshifts were calculated using both aperture and isophotal photometry. There were 86 galaxies that had "good" spectroscopic redshifts as defined by Cohen [6]. Figure A.12 is a plot of photometric redshifts calculated with aperture photometry against spectroscopic redshift. Figure A.13 is a plot of photometric redshifts calculated with isophotal photometry against spectroscopic redshift.

There is no difference between photometric redshifts computed from aperture photometry and photometric redshifts computed from isophotal photometry for galaxies for which we have spectroscopic redshifts. The median difference between photometric and spectroscopic redshifts for aperture photometry is $z_{\text{spectroscopic}} - z_{\text{photometric}} = 6 \times 10^{-3}$. The median difference between photometric and spectroscopic redshifts for isophotal photometry is $z_{\text{spectroscopic}} - z_{\text{photometric}} = -8 \times 10^{-4}$. In both cases, the median difference is essentially zero. The dispersion of the difference for aperture photometry is 9×10^{-2}, while for isophotal photometry the dispersion is 9×10^{-2}. Therefore, both photometry methods produce identical photometric redshifts for the galaxies for which spectroscopic redshifts are available. This result is expected because both photometric methods should produce identical results for bright objects. The galaxies with spectroscopic redshifts are bright because more photons are needed to resolve spectra than to resolve an image.

Because the galaxies for which we have spectroscopic redshifts were unrevealing, the next step was to compare the difference between photometric redshifts for the entire catalog. Figure A.14 is a plot of $z_{\text{aperture}} - z_{\text{isophotal}}$ versus isophotal magnitude. The spread in $z_{\text{aperture}} - z_{\text{isophotal}}$ increases as the galaxies get fainter. This result is not surprising because Figure A.11 shows that the magnitudes measured by each method differ more as the flux of the sources decreases. However, Figure A.14 does not indicate the presence or absence of a systematic redshift divergence between the two methods.

There is no systematic divergence between isophotal photometric redshifts and aperture photometric redshifts. Figure A.15 is a plot of the median of the difference between z_{aperture} and $z_{\text{isophotal}}$, the dispersion of that difference, and the median redshift uncertainty versus isophotal magnitude. The median difference between photometric redshifts remains nearly zero for all magnitudes and never rises above the uncertainty in redshift. There is no systematic difference between isophotal and aperture photometric redshifts.

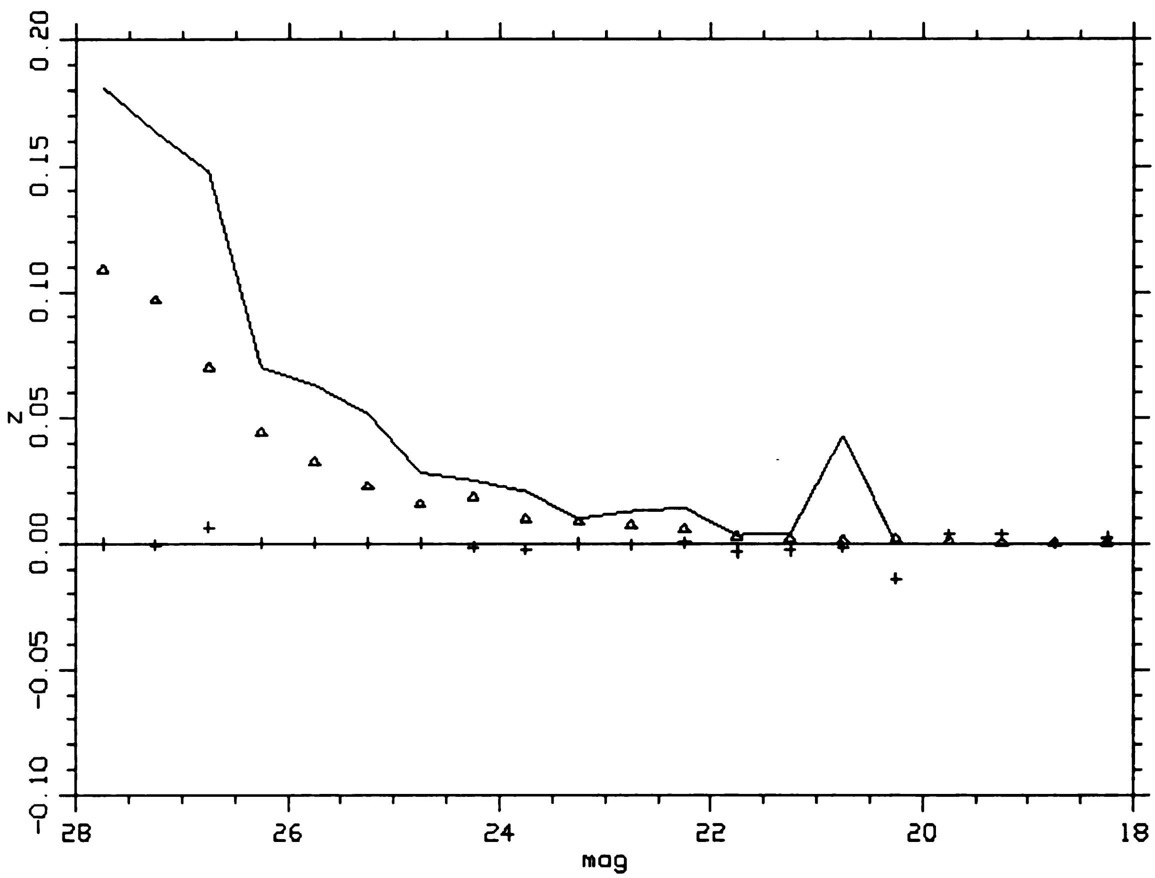

Figure A.15: The median difference between photometric redshifts calculated with aperture and isophotal photometry (+), the dispersion of the median difference (-), and the median uncertainty of the differences ($\triangle$) in each bin plotted versus aperture magnitude for 976 galaxies in the HDF. The data are grouped into bins 0.5 magnitudes wide.

A.2.6 Conclusion

There is no bias between redshifts created with isophotal photometry and aperture photometry. There is a consistent magnitude difference between isophotal photometry and aperture photometry for faint objects. Therefore, the luminosity function will determine the choice of photometry method.

The luminosity function of a survey of galaxies is a measure of galaxy density with respect to magnitude in a given volume of space. Figure A.11 shows that the magnitudes of bright galaxies are acceptable with isophotal photometry, but the magnitudes of less luminous galaxies are consistently too faint. This error creates a luminosity function that is artificially low for faint galaxies. Aperture photometry will be used in further work to calculate photometric redshifts to prevent this deficit in the luminosity function.

In conclusion, aperture photometry is the desired photometry method because it does not systematically exclude light from faint galaxies. The correct luminosity function of a galaxy sample may be determined from aperture photometry.

Bibliography

[1] Bertin, E. & Arnouts, S. 1996, A&AS, 117, 393

[2] Biretta, J., *et al.* 2001, WFPC2 Instrument Handbook, Version 6.0 (Baltimore:STScI)

[3] Brainerd, T., Blandford, R., & Smail, I. 1996, ApJ, 466, 623

[4] Broadhurst, T.J., Taylor, A.N., & Peacock, J. A. 1995, ApJ, 438, 49

[5] Code, A. 1959, PASP, 71, 118

[6] Cohen, J., *et al.* 2000, ApJ, 538, 29

[7] Efstathiou, G., Ellis, R. S., & Peterson, B. A. 1988. MNRAS, 232, 431

[8] Einstein, A. 1936, Science, 84, 506

[9] Fernandez-Soto, A., Lanzetta, K.M., & Yahil, A. 1998, ApJ, 513, 34

[10] Fischer, P., *et al.* 2000, AJ, 120, 1198

[11] Folkes, S., *et al.* 1999, MNRAS, 308, 459

[12] Fort B., Mellier Y., & Dantel-Fort M., 1997, A&A, 321, 353

[13] Fukugita, M., & Turner, E. 1991, MNRAS, 253, 99

[14] Jacoby, G., *et al.* 2000, NOAO CCD MOSAIC Imager Manual (Tucson:NOAO)

[15] Januzzi, B.T., & Dey, A. 1999, ASP Conference Series, 191, 111

[16] Januzzi, B.T. 2002, private communication

[17] Kennicutt, R.C. 1992, ApJS, 79, 255

[18] LaCluyzé, A.P. 2002, private communication

[19] Lanzetta, K.M., Yahil, A., & Fernandez-Sota, A. 1996, Nature, 381, 759

[20] Lilly, S.J., Tresse, L., Hammer, F., Crampton, D., & Le Fevre, O. 1995, ApJ, 453, 108

[21] Loh, E. & Spillar, E. 1986, ApJ, 303, 154

[22] Mayen, C. & Soucail, G. 2000, A&A, 361, 415

[23] Refsdal, S. 1964, MNRAS, 128, 295

[24] Rögnvaldsson, Ö.E., *et al.* 2001, MNRAS, 322,131

[25] Schecter, P. 1976, ApJ, 203, 557

[26] Taylor A.N., Dye S., Broadhurst T.J., Benitez N., & Van Kampen E., 1998, ApJ, 501, 539

[27] Tully, R.B. & Fisher, J. R. 1977, A&A, 54, 661

[28] Tyson, J.A., Valdes, F., Jarvis, J.F., & Mills, A.P. 1984, ApJ, 281, L59

[29] Williams, R.E., *et al.* 1996, AJ, 112, 1335

[30] Wilson, G., Kaiser, N., Luppino, G., & Cowie, L. 2001, ApJ, 555, 572

[31] Young, P., Gunn, J., Kristian, J., Oke, J.B., & Westfall, J. 1980, ApJ, 241, 507